

Computational and Experimental Analysis of Gas/Liquid Two-Phase Flow in Rod Bundles with Mixing-Vane Spacer Grids

Brian M. Waite^{a,1}, Horst-Michael Prasser^b, and Michael Z. Podowski^a

^a*Rensselaer Polytechnic Institute, Center for Multiphase Research, 110 8th Street, Troy 12180*

^b*ETH Zurich, Laboratory of Nuclear Energy Systems, ML K 19, Sonneggstrasse 3, 8092 Zurich, Switzerland*

Abstract

The existing evidence clearly shows that the physical phenomena governing gas/liquid two-phase flows are quite complicated even in the case of smooth conduits and simple geometries. Needless to say, the development of experimental, analytical and computational methods for predicting such flows in complex geometries is a much more complicated and challenging task. A configuration of interest to a broad range of industrial applications, including nuclear reactors, deals with the flow of two-phase mixture along the channels formed between narrow arrays of multiple parallel cylindrical elements (tubes or rods). The alignment of such elements is normally accomplished by installing spacer grids placed at regular distances along the flow. The presence of spacers actually affect flow conditions, including the velocity field, pressure drop, heat transfer and, in the case of two-phase flows, phase distribution.

The objective of this paper is to present a comparative analysis of the results of a combined experimental, theoretical, and computational study of phase distribution around and downstream from complex-geometry spacer grids with split-vane type mixing devices. The main emphasis has been given to the analysis of the effect of proper interpretation of the experimental data on the modeling consistency, the understanding of uncertainties and limitations associated with the results of multidimensional computer simulations performed using mechanistic modeling principles based on an average bubble size.

Keywords: Rod Bundle with Spacer Grids, Gas/Liquid Flow, Void Fraction Measurements with Wire Mesh Sensor, Multi-field Model, Experimental Model Validation

1. Introduction

Whereas the main purpose of using spacer grid in parallel-rod bundles is to assure that proper alignment is maintained between the neighboring rods, their potential impact of flow and temperature fields, as well as on phase distribution provides an excellent opportunity for the optimization of system performance by appropriate designs of spacer geometry. One such design concept deals with the addition of mixing vanes. A typical geometry of a rod bundle with a split-vane spacer grid is shown in Figure 1. Neighboring vane pairs are alternated in orientation to promote cross-flow between subchannels. Similar geometries are used in a variety of both single-

¹ Corresponding Author

Email addresses: waiteb15@gmail.com (Brian M. Waite), prasser@lke.mavt.ethz.ch (Horst-Michael Prasser), podowm@rpi.edu (Michael Z. Podowski),

phase and two-phase systems in general, and pressurized water nuclear reactors (PWR) in particular.

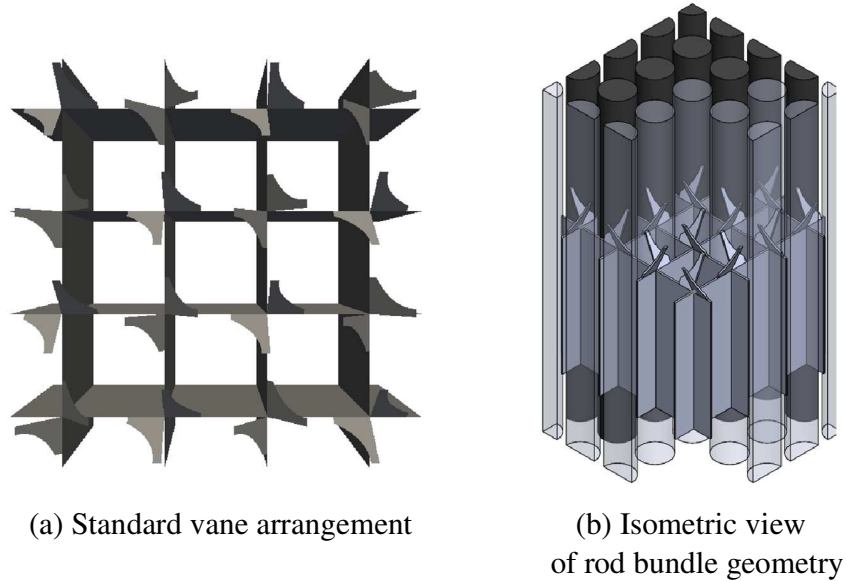


Figure 1. Rod bundle spacer grids used in this study.

The complexity of spacer geometry makes it very difficult to capture details of the highly-localized swirl flow and mass redistribution downstream from the spacer. The majority of both experimental and computational studies performed to date have been limited to single-phase flows (Karoutas et al., 1995; McClusky et al., 2003; Holloway et al., 2005; Dominguez Ontiveros, 2012, Conner et. al, 2016, Nguyen and Hassan, 2017, Busco and Hassan, 2018, Busco et al, 2019), so that the impact of the spacer on void distribution in two-phase flow is not fully understood.

One of very few experimental investigations addressing the effect of spacer grids on two-phase flow was conducted by Ylönen (2013) using the SUBFLOW facility at Paul Scherrer Institute in Switzerland. Whereas the results of the study have demonstrated that the wire-mesh-sensor-based measurement technique is capable of capturing local distribution of void fraction around spacers, the very nature of this technique is inherently associated with several sources of potential uncertainties. Nevertheless, when properly interpreted, the SUBFLOW experimental data should become a very useful source of reference for model validation.

Typical model-validation efforts normally focus on either comparing a fixed-parameter model against specific experimental data or adjusting selected parameters or modeling assumptions to best match such data. The former approach have been applied to selected SUBFLOW results by Goodheart et al. (2014) using the commercial CFD code, STAR-CCM+. A common feature of both approaches is the implicit assumption that the results of measurements are the unique true values. Since this is normally not the case in two-phase flow systems, as experimental uncertainties can be quite large, a complete assessment of models predictive capabilities requires that a comprehensive understanding of the combined experimental and modeling uncertainties be achieved.

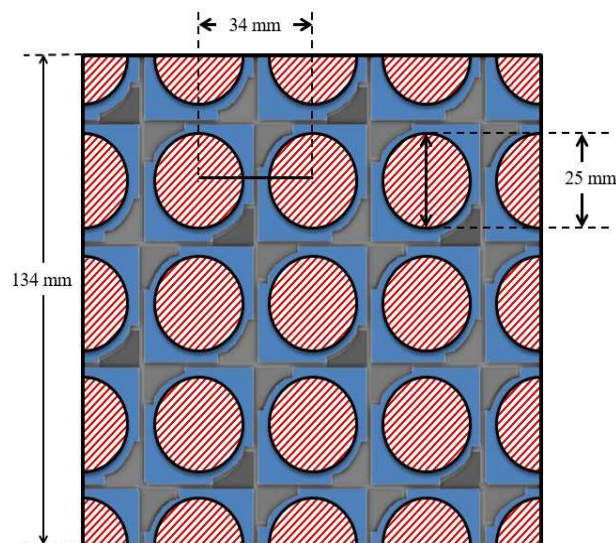
The objective of this paper is to present the results of such an analysis using as a reference the flow data of Ylönen (2013). Two different processing methods for the same experimental data are presented in the first part of the paper, and the resultant differences are analyzed from the

perspective of measurement uncertainties. The second part of the paper gives a description of a Computational Multiphase Fluid Dynamics (CMFD) model used in the computer simulations of the SUBFLOW experiments. A comparison between the predictions and data is shown in the last part of the paper, including a discussion of the combined experimental and modeling uncertainties and of their interpretation in the assessment of model's consistency and accuracy.

2. SUBFLOW Facility

The SUBFLOW facility at the Paul Scherrer Institute (PSI) has been designed to investigate complex flow phenomena in rod-bundle flows. The acrylic-rod bundle created 4×4 interconnected subchannels that were subject to two-phase flow. As it can be seen in Figure 2, the bundle model represents a sub-bundle geometry cut out of an undisturbed rectangular lattice of rods, whereby the cut is performed along lines through the subchannel gaps where a minimum of unrealistic no-slip boundary conditions is added. The result is a geometry consisting of 3×3 full cylindrical rod simulators, 3×4 half-cylinders at the edges of the sector and 4 quarter rods in the corners. In the sum, these rod simulators thus represent $3 \times 3 + 4 \times 3 / 2 + 4 \times 1 / 4 = 16 = 4 \times 4$ full rods. The working fluid entered the facility shown in Figure 3 from the bottom and exited it from the top. The bubbles were injected in the center of each individual subchannel using 16 collocated air-capillary outlets. The wire mesh sensor (WMS) has been located 1,915 mm from the inlet. A partial spacer has been installed 912 mm upstream of the wire-mesh sensor on the outer rods to provide extra structural support (details can be found in Ylönen et al. (2011)). Figure 2 shows a lateral view of the 4×4 channel rod bundle with the spacer grid.

The experiments with spacer grids used a movable spacer with split-vane type mixing vanes that was held in place by fixing pins that could be removed from the outside, after which the spacer grid could be moved magnetically in 50 mm increments when the flow is off. Dimensions of the spacer grid have been taken from the paper of Navarro and Santos (2009). The data was recorded at four different spacer locations, which correspond to the distance from the top of the spacer to the WMS. The nominal conditions for the experiments with spacer grids are outlined in Table 1. The measurements without spacer grids are assumed to be close to a fully-developed flow condition in the rod bundle.



2.1. Wire Mesh Sensor

The measurements made in these experiments were taken with a pair of two-layer wire mesh sensors which uses the local conductivity of the fluid at the crossing points of the wires to determine parameters such as void fraction and bubble velocity. The data reduction of the raw measurements can introduce slight uncertainties that will be discussed in Section 2.3.

The sensor operates at 2.5 kHz, which allows for a high time resolution. The WMS was made of wires that were threaded through the rods to cover the cross-section of the subchannel with a dense matrix of measuring positions. The crossing points of wires within the acrylic rods were ignored during post processing. The 64x64 grid of wires with a pitch of 2.125 mm provided 2,304 unique measurement locations within the flow area of each layer. In each of the 16 subchannels, a matrix of 16x16 grid points was accommodated, from which 144 were fully outside the cross-sections of the rods. The applied pitch only allows a bubble to be recognized with a minimum diameter of about 2 mm. The two wire sensors were placed 15 mm apart from one another in order to get a reasonable distance with minimal errors for the time-of-flight calculations used for the bubble velocity measurements.

The pair of two-layer sensors allows for the evaluation of bubble velocity when the two signals are cross-correlated. While it has been well documented that the first sensor may cause bubble fragmentation and other disturbances, the signal recorded by the first sensor is consistent with information obtained by high-speed camera imaging (Prasser et al., 2016) and still represents the structure of the two-phase flow before the sensors. Furthermore, WMS measurements of void fraction and bubble size have been shown (Prasser et al., 2005) to be consistent with data measured with ultra-fast X-ray tomography. More details on this specific sensor have been discussed by Ylönen (2013).

2.2. Air Injector

The air injector used in the SUBFLOW facility was specifically designed for this experiment based upon previous investigations (Milenković, 2005). The injector has 16 water tubes with coaxial air capillary outlets that inject bubbles into the liquid flow at the center of each subchannel which is controlled by volumetric flow rate (schematic of injector is shown in Ylönen, 2013). A secondary liquid flows in an annulus outside the air capillary. Varying the rate of secondary liquid flow allows the control of the bubbles conditions injected into the test section. An increase in the secondary flow rate, while keeping the airflow constant, increases bubble departure frequency and decreases bubble size. For the measurements in this experiment, this flow rate was kept constant at 1000 l/hr (62.5 l/hr per channel). The secondary liquid flow is taken from the primary liquid flow in order to keep the total liquid flow consistent.

The SUBFLOW experiments (Ylönen, 2013) show that higher airflow cases have a larger spread of bubble sizes as the standard deviation of bubble sizes increased. Therefore, only the cases with smaller airflow rates exclusively exhibit small bubbles near the walls of the subchannels.

It is important to notice that there is no control of bubble size once the bubbles have left the air injector. Whereas in principle, larger bubbles may experience breakup and/or coalescence as along the flow, the impact of such phenomena was apparently very small in both the bare SUBFLOW bundle and downstream from the spacer since the void fraction was very low. At the

same time, the spacer grids have caused a significant bubble breakup. Details in this regard, including the impact on the accuracy of model's predictions, are discussed in Section 5.

2.3. Data Processing

As it was earlier stated, raw local conductance readings must be post processed into void fraction and bubble velocity data. Bubble identification algorithms are used to detect bubbles and determine their diameter, which allowed for the calculation of population statistics. A theoretical study of the uncertainty of this data reduction method was presented by Prasser and Häfeli (2018) who applied potential field simulations to predict the response of the wire-mesh sensor to a passage of a gas bubble. As a result, a new data processing method was proposed. The differences between the newer methods and those used by Ylönen (2013) will be shown here.

The pitch of the wires used in the experiment, i.e., 2.125 mm, is used as a frame of reference for converting the crossing point indexes to x and y coordinates. The measurement frame index (instance in time), k , and the frequency of the system convert to the time of measurement as shown here

$$x = i \cdot \Delta x \quad y = j \Delta y \quad t = k \cdot \Delta t_{\text{meas}} = \frac{k}{f_{\text{meas}}} \quad (1)$$

The methods used by Ylönen (2013) convert the measured conductance into a local instantaneous void fraction using a calibrated conductivity of plain water and the conductivity of gas assuming a linear relationship as shown below

$$\alpha_{i,j,k} = 1 - \frac{I_{i,j,k} - I_{\text{gas},i,j}}{I_{\text{water},i,j} - I_{\text{gas},i,j}} = 1 - \frac{I_{i,j,k}}{I_{\text{water},i,j}} \quad (2)$$

where the simplified form sets the conductivity of the gas to be zero. Furthermore, deviations from the liquid conductivity lower than 10% have been filtered out as disturbances of that size could be attributed to electrical noise. The filter is applied by checking the six neighbors of all void fraction values lower than 10%. If a neighbor has a void fraction above 10%, it is assumed to be part of a bubble and the contribution is meaningful. If none of the neighbors has a void fraction above 10%, it is assumed nonphysical and the value is set to zero. Negative local instantaneous void fraction values below zero were corrected to zero as it was assumed that negative values lack physical meaning. The method will hereinafter be referred to as the “linear cut” method. In reality, this procedure could have resulted in neglecting some signals caused by the actual bubbles.

Two-dimensional distributions of the time averaged void fraction is found by a simple averaging over all measurement frames, k , in the 20 second run, which gives a void fraction data point for each lateral location in the flow, given by

$$\bar{\alpha}_{i,j} = \frac{1}{n} \sum_{k=1}^n \alpha_{i,j,k} \quad (3)$$

This averaged void fraction is most interesting for the steady-state RANS CFD validations reported in Section 5.

Ylönen (2013) used a separate calibration run of pure demineralized water to determine the conductivity of water. This methodology could introduce uncertainties if the air/water mixture changed the baseline of conductivity throughout the course of the run. For the interpretation of the experimental data presented in this paper, calibration has been completed for each run using

the probability distribution functions (PDF) of the conductance calculated individually for every position within the measuring matrix of sensor. The conductivity of plain water was found by a search of the maximum of each individual PDF. This approach delivers valid calibration data as long as a low-void bubbly flow is present, with large periods of the presence of the liquid phase between gas bubbles. This allowed one to extract a more representative average liquid conductance during the multiphase run.

As it has been mentioned before, Prasser and Häfeli (2018) have tested the “linear cut” method with the help of potential field calculations. They have shown that an omission of the conductance overshoots leads to an overestimation of bubble size and void fraction. At a crossing point between the transmitter and receiver wire (which is close to another crossing point, partially covered by the liquid phase) the measured conductance may exceed the conductance sampled during calibration with plain liquid. This excess conductance is due to a breaking of the symmetry in the electrical potential field around the wires present before the incidence of gas-liquid interface. The resulting overshoot is equivalent to an apparent negative void fraction, which reflects a real excess of liquid that is not accounted for in the partially filled measuring location. It can be accounted for by using a “no cut” method, where the negative void fraction values are included in the averaging and thus reduce the integral void fraction according to the quantity of excess liquid. This has been shown to be more representative of the true void fraction and the true bubble volume.

The “no cut” approach requires the redistribution of the excess conductance from cells with an overshoot to neighboring cells with a deficit due to the mentioned symmetry breakage. This was done by shifting the excess conductance to the neighboring cell with the lowest conductance thus with the highest local instantaneous void fraction. If this cell cannot receive the entire excess, because its initial conductance is too high to fully accommodate it, the rest of it will be given to the neighbor with the second lowest conductance, and so forth. The results of this procedure are shown in Figure 4.

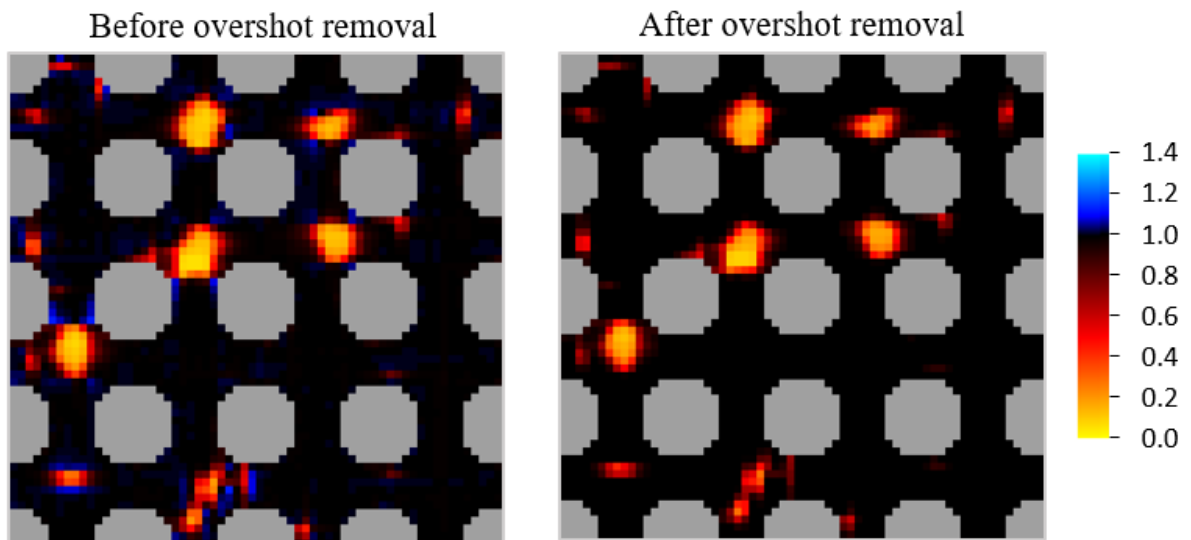


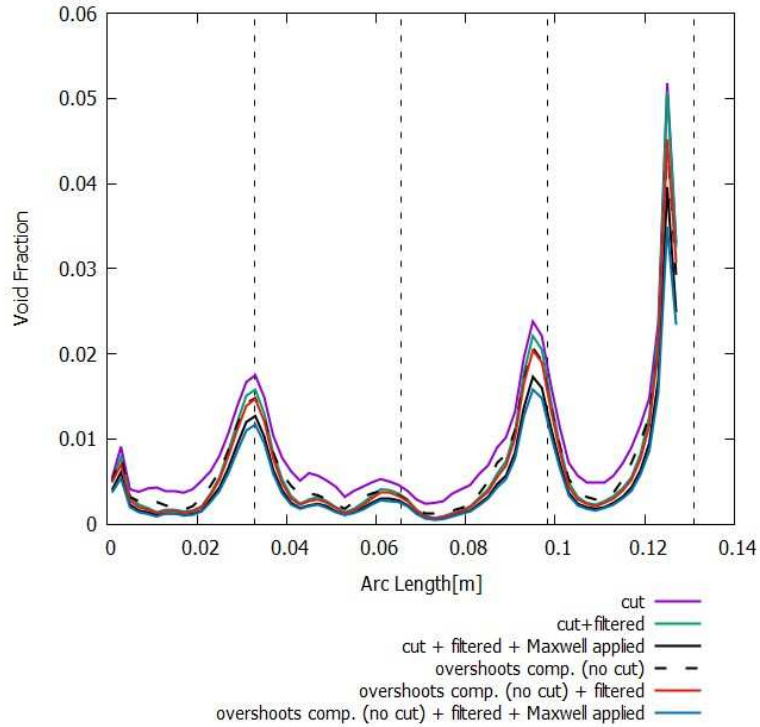
Figure 4. Arbitrary snapshots of instantaneous sensor signals before and after overshoot removal.

In the same paper, it has also been found that the linear relationship between void fraction and conductance is not the best approximation. The non-linear Maxwell relationship between

void and conductance has lower systematic errors in estimating bubble volume and void fraction, as given by

$$\alpha_{i,j,k} = \frac{1 - \left(I_{i,j,k} / I_{water,i,j} \right)}{1 + \frac{I_{i,j,k} / I_{water,i,j}}{2}} \quad (4)$$

While these improvements are important and necessary, it points to the inherent uncertainties in the experimental methods. A systematic analysis of the different data reduction methods provides information on how each method influences the final answer. Figure 5 shows the stepwise impact of the changes from the old methods to the new method for cases 1-1 and 3-2. All of the calculations in Figure 5 use the PDF liquid conductivity calibration method. The void data is plotted in all calculations across the rod gap for the experiment without spacer's, averaging the two center locations. The six different lines in each plot represent a combination of the steps discussed above. The “cut” indicates that the values below zero are excluded instead of values below 10%. “Maxwell” means that the void fraction has been calculated using Eq.(4). “Overshoots compensated” is used when the filter is not enacted. After the cut has been enacted or the “overshoots” have been compensated for, there are still some negative values that need to be removed since they cannot be interpreted as neighbors of bubbles. This has been referred to as the “filtered” in Figure 5.. The step “cut+filtered” most closely represents the “Linear cut” method, and the “overshoots+filtered+Maxwell” represents the “Maxwell no cut” method in Figure 5. The application of the “Maxwell” relationship versus the “linear” method seems to provide the largest effect. Figure 5 shows that the results for “cut+filtered+Maxwell” is only slightly higher than “overshoots+filtered+Maxwell”. The figures show the different steps change the final void fraction value by about 20-50%. Comparing the “overshoot+filtered+Maxwell” step with just the “overshoot+filtered” (linear) method has a significant reduction of about 25% on the void fraction data further showing “Maxwell” vs “linear” is a significant factor. Additional comparisons between both methods are shown in Section 5.



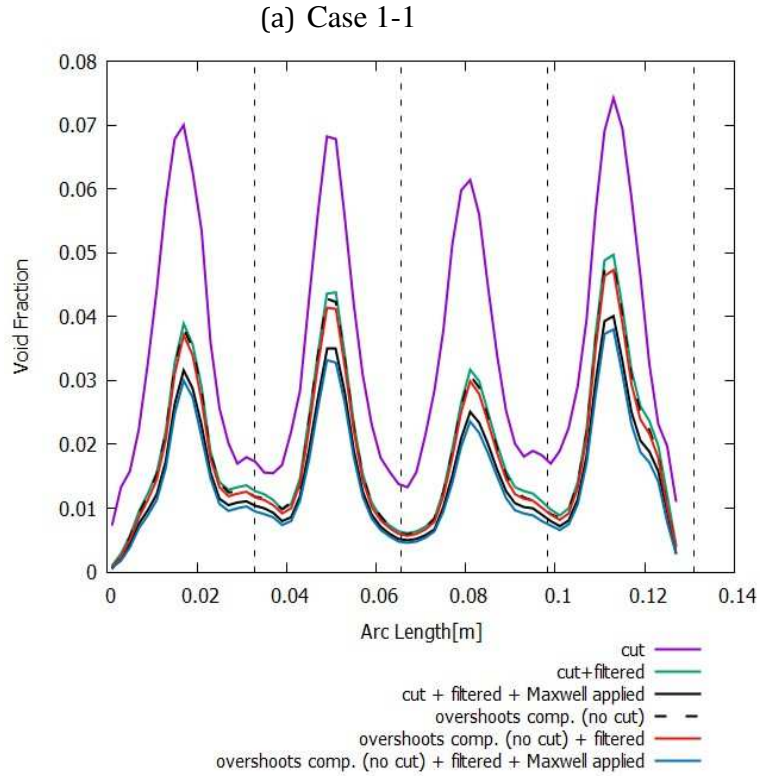


Figure 5. Effects on void by the improvements in data reduction.

In a quantitative assessment of the measured average void fraction, it has been compared against the correlation of Liao et al. (1985) contained in the drift-flux model. This correlation has been compared to a large number of experimental data stemming from measurements in smooth bundles by Coddington and Macian (2012) and found to be one of the three best performing formulae over a wide range of void fractions and system parameters. For the purpose of this comparison, we averaged the readings of the wire-mesh sensor over the free flow cross-section. The result is shown in Figure 6. The comparison was carried out for all different combinations of superficial velocities that were used by Ylönen in the bare bundle ($j_l = 0.8, 1.2, 1.6 \text{ m/s}$; $j_v = 0.008, 0.02, 0.039, 0.059 \text{ m/s}$). Also shown are the corresponding values calculated using the current two-fluid model discussed in Section 3 compared to the “Maxwell No Cut” experimental data. The improvement by the “Maxwell No Cut” method over the “Linear Cut” is evident. The experimental points with void fractions below 2 % display a nearly ideal match with the correlation of Liao for a bubbly flow. At higher void fractions, the experiment gave slightly lower void fractions, which is coherent with the findings of Coddington and Macian (2012).

Overall, the uncertainties in the local void fraction measurements are of the order of 5-10%, and in the average void fraction they do not exceed 5-6%. This is consistent with the results of a previous study (Tompkins et al., 2018) entirely focused on the uncertainty analysis for wire-mesh sensors. Given the impact of the randomness of bubble trajectories at low void fractions at the average local gas concentration, the results of the measurements constitute a solid and consistent data base for model validation.

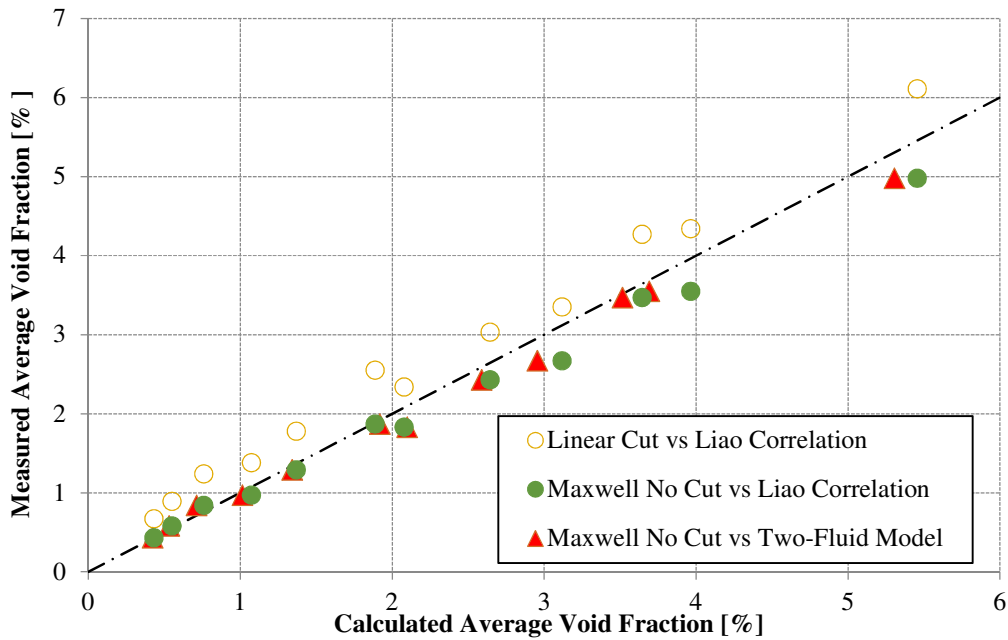


Figure 6. Comparison of average void fractions with 1-D void calculations

3. Multiphase Flow Modeling

3.1. Multi-field Modeling Framework

Multiphase flow models can be formulated using a number of different methods and scales, from DNS/Interface-tracking methods to the ensemble-averaged multi-field or two-field approaches. To properly assess the predictive capabilities of any model by comparing the results of calculations against specific experimental data, it is important to recognize that such data is always associated with numerous physical uncertainties, as well as those associated with the both the instrumentation and the data processing method (see Section 2). The effect of the complexity of the physical characteristics of gas/liquid two-phase flows on the interpretation of experimentally-collected data for modeling purposes is mainly associated with:

- Random distribution of bubble sizes.
- Degree of bubble deformation.
- Continuous phase (liquid) turbulence in gas/liquid two-phase flow.
- Bubble-induced turbulence.
- Bubble/liquid interfacial momentum transfer.
- Uncertainties in the measured (or assumed) fluid properties.
- Volumetric phase change rate (boiling and/or condensation) in heated channels.
- Bubble/liquid interfacial heat transfer.
- Gas injection mode and vapor formation rate at heated surface.
- Surface/fluid interactions at micron or nano level.

Furthermore, since the results of model predictions are normally based on computer simulations, the results of such simulations are affected by the accuracy of computational methods. Example of the underlying issues are:

- Effect of interface tracking method (in micro-scale simulations such as DNS).
- Effect of bubble size on computational grids (mainly in RANS-level simulations).
- Effect of complex local geometries.

Whereas the coupled DNS(LES)/Interface-Tracking methods, which can directly model flow turbulence, have a lot of advantages due to their ability to capture small-scale details, their application to practical engineering problems, in particular to two-phase flows at high Reynolds numbers and in complex geometries, still encounters serious limitations. At the same time, the ensemble-averaging multi-field model, which is based on the RANS-level modeling of turbulence, turns out to be numerically efficient and, if formulated in a consistent manner, is capable of capturing major phenomena governing the fluid mechanics and heat transfer of gas/liquid flows for a variety of situations and systems.

The single-phase Navier-Stokes equations, given by

$$\frac{\partial \rho}{\partial t} + \nabla \cdot (\rho \bar{u}) = 0 \quad (5)$$

$$\frac{\partial}{\partial t} (\rho \bar{u}) + \nabla \cdot (\rho \bar{u} \bar{u}) = -\nabla P + \nabla \cdot \underline{\underline{\tau}} + \rho \bar{g} \quad (6)$$

are based on the first-principle fluid continuum concept, and can be readily used in DNS simulations for a fluid of given properties, as long as the fluid/wall boundary conditions are well-defined. In the case of two-phase flows, Eqs.(6)-(7) must be complemented by an interface tracking model. Since such models are based on simplifying assumptions, the resultant combination is actually no longer a first-principle type. Naturally, such models have been successfully used to investigate details of gas/liquid interactions in two-phase flows for different physical situations (e.g., see Bolotnov et al. (2010), Behafarid et al. (2013)), but they are normally associated with profound numerical issues which limit their applications. Furthermore, the nature of micro-scale interactions between gas, liquid and conduit walls may still require that additional closure models be used (e.g., to account for the ultra-thin liquid film which prevents bubbles from touching the wall (Behafarid et al., 2015)).

The RANS-level models are based on ensemble-averaging the governing equations, Eqs.(5)-(6), over the entire two-phase flow domain (Delhay, 1981; Lahey, Jr. and Drew, 1988). One of the most successful approaches uses the interpenetrating-fluids concept, which leads to the multi-field model, formulated in a stationary (Eulerian-Eulerian) frame of reference. The major assumption behind the multi-field model is that all component fluids are equal partners and each, if considered separately, is governed by Eqs.(5)-(6). Examples of such gas/liquid flows are a stratified flow or an annular flow pattern without dispersed droplets. However, it has been shown (Podowski, 2009) that the ensemble-averaging of gas/liquid bubbly flows yields the momentum equation for the dispersed-bubble field which is inconsistent with the interpenetrating fluid concept. Thus, additional analysis (and assumptions) are still needed to arrive at the following well-established multi-field form of the continuity and momentum equations for gas/liquid bubbly flows (Podowski, 2009),

$$\frac{\partial}{\partial t} [(1-\alpha)\rho_l] + \nabla \cdot [(1-\alpha)\rho_l \bar{u}_l] = 0 \quad (7)$$

$$\frac{\partial}{\partial t} (\alpha_{v,k}\rho_v) + \nabla \cdot (\alpha_{v,k}\rho_v \bar{u}_{v,k}) = 0 \quad (k=1, \dots, K) \quad (8)$$

$$\frac{\partial}{\partial t} [(1-\alpha)\rho_l \bar{u}_l] + \nabla \cdot [(1-\alpha)\rho_l \bar{u}_l \bar{u}_l] = -\alpha \nabla P + (1-\alpha) \nabla \cdot \underline{\underline{\tau}}^{tot} + (1-\alpha)\rho_l \bar{g} + \bar{M}_{v-l}^i \quad (9)$$

$$\frac{\partial}{\partial t} (\alpha_k \rho_v \bar{u}_{v,k}) + \nabla \cdot (\alpha_k \rho_v \bar{u}_{v,k} \bar{u}_{v,k}) = -\alpha_k \nabla P + \alpha_k \nabla \cdot \underline{\underline{\tau}}^{tot} + \alpha_k \rho_v \bar{g} + \bar{M}_{l-v,k}^i \quad (k=1, \dots, K) \quad (10)$$

where

$$\alpha = \sum_{k=1}^K \alpha_k \quad (11)$$

$$\vec{M}_{v-l}^i = -\vec{M}_{l-v}^i = -\sum_{k=1}^K \vec{M}_{l-v,k}^i \quad (12)$$

In the above equations the subscripts, l and v , respectively, refer to the liquid and gas phases, k is the bubble group size indicator, α_k is the volumetric concentration of bubble group- k , $\underline{\underline{\tau}}^{tot}$ is the total shear stress, $\vec{M}_{l-v,k}^i$ is the total interfacial force per unit volume by the liquid field on bubble field- k , and the remaining notation is conventional.

Whereas the form of Eqs. (7)-(12) is consistent with the fundamental principles of fluid mechanics, they must be complemented by two major groups of closure laws, one for the total shear stress, the other for the interfacial forces.

At the RANS-level formulation, several local turbulence models have been developed for single-phase flows. They have been extended to two-phase flows, but several issues still remain open. A typical approach is to express the shear stress in terms of the total viscosity of the continuous liquid field, which is a superposition of the combined molecular (ν_l) and turbulent viscosity (ν_l) of this field, and the bubble-induced viscosity (ν_{Bl}), i.e.

$$\underline{\underline{\tau}}^{tot} = \rho_l (\nu_l + \nu_t + \nu_{Bl}) \nabla \vec{u}_l \quad (13)$$

The turbulent eddy viscosity can be determined from one of a number of existing models. It is important to realize that the choice of a specific model should be consistent with the fact that the presence of bubbles dramatically changes the near-wall distribution of the liquid field parameters normally used to characterize turbulence at the RANS level (Bolotnov and Podowski, 2012). In particular, using well-tuned single-phase turbulence models, such as the Low-Reynolds Number $k-\varepsilon$ model, may lead to significant inconsistencies and inaccuracies. As it has been shown before, using a High-Reynolds Number $k-\varepsilon$ model applied to a computational mesh consistent with the bubble size is an approach consistent with other modeling uncertainties. Such an approach has been used in this study. It has been combined with the bubble-induced turbulence model proposed by Sato et al. (1981).

The total interfacial force for each bubble group, $\vec{M}_{l-v,k}^i = -\vec{M}_{v,k-l}^i$, accounts for the momentum transfer between the individual fluids. A common approach is to assume that the total force is a superposition of various component forces. Whereas, theoretically, several forces have been identified and modeled with varying degrees of detail and generality, it is important for the consistency of the overall model that appropriate filtering be used to eliminate less important or relevant forces, and leave only the most important ones which are based on mechanistic principles. With this in mind, and using the past experience, the total interfacial force has been partitioned into four major components (Podowski, 2009)

$$\vec{M}_{l-v,k}^i = \vec{M}_{l-v,k}^D + \vec{M}_{l-v,k}^{VM} + \vec{M}_{l-v,k}^L + \vec{M}_{l-v,k}^{TD} \quad (14)$$

where $\vec{M}_{l-v,k}^D$ is the drag force, $\vec{M}_{l-v,k}^{VM}$ is the virtual mass force, $\vec{M}_{l-v,k}^L$ is the lift force and $\vec{M}_{l-v,k}^{TD}$ is the turbulent dispersion force, all exerted by the liquid field on gas field- k . The individual forces are discussed below.

3.2. Drag Force

The drag force acts in the direction opposite to the movement of particles passing through a stationary or moving fluid. Performing ensemble averaging gives the following relationship

$$M_{l-v,k}^D = -\frac{1}{8} C_{D,k} \rho_l |\bar{u}_{r,k}| \bar{u}_{r,k} A_k^{mi} \quad (15)$$

where $C_{D,k}$ is the drag coefficient for bubble group- k , $\bar{u}_{r,k} = \bar{u}_{v,k} - \bar{u}_l$ is the corresponding gas-to-liquid relative velocity, $A_k^{mi} = 6 \frac{\alpha_k}{d_{b,k}}$ is the interfacial area density for the group- k bubbles, and $d_{b,k}$ is the corresponding equivalent bubble diameter.

The drag coefficient needs to be determined appropriately for any given situation. In particular, $C_{D,k}$ depends on flow conditions and bubble size, and can typically be evaluated from various experimentally-based expressions. For spherical bubbles, an updated form of the formulation originally proposed by Ishii and Mishima (1984) can be used

$$C_{D,k} = \frac{24}{\text{Re}_{b,k}} \left(1 + 0.092 \text{Re}_{b,k}^{0.78} \right) \quad (16)$$

where

$$\text{Re}_{b,k} = \frac{|\bar{u}_{v,k} - \bar{u}_l| d_{b,k}^{eff}}{\nu_l} \quad (17)$$

For distorted bubbles, a well-documented formula has been proposed by Zuber-Findley (1965), given by

$$C_{D,k} = 0.57 d_{b,k} \sqrt{\frac{g(\rho_l - \rho_v)}{\sigma}} (1 - \alpha)^2 \quad (18)$$

Another expression has been proposed by Ishii and Mishima (1984) as

$$C_{D,k} = \frac{2d_{b,k}}{3} \sqrt{\frac{g\Delta\rho}{\sigma}} \left\{ \frac{1 + 17.67 \left[(1 - \alpha)^{1.5} \right]^{6/7}}{18.67 (1 - \alpha)^{1.5}} \right\}^2 \quad (19)$$

It is interesting to notice that when applied to a single bubble under the condition, $\rho_v \ll \rho_l$, Eq.(18) yields a commonly used expression for the terminal rise velocity of deformed bubbles

$$u_\infty = 1.53 \left(\frac{g\sigma}{\rho_l} \right)^{0.25} \quad (20)$$

This, in turn, provides an assurance that Eq.(18) is applicable to low relative gas volumetric flow rates. On the other hand, Eq.(19) over predicts the bubble rise velocity by almost 20%.

Another important observation in regard to Eq.(18) and Eq.(19) is that both of them refer to a conduit-cross-section averaged void fraction, so their direct application to flows experiencing high lateral void gradients may have a negative impact on the accuracy of calculations and should thus be approached with caution.

As can be noticed from Eq.(16), the drag coefficient for small bubbles is a nonlinear function of bubble diameter. At the same time, both Eq.(18) and Eq.(19) indicate that for deformed (or distorted) larger bubbles and low gas volumetric flow rates fractions, the ratio of drag coefficient to bubble diameter is nearly constant, especially for low void fractions. For instance, in the current case SUBFLOW experiment 3-1, performed for air/water flow at room temperature with $\alpha < 0.05$ (see Table 1) and $\alpha_{av} = 0.035$ (see Figure 6) Eq.(18) yields, $C_{D,k} / d_{b,k} \approx 195$.

It is important to notice that the accuracy of predictions using both Eq.(18) and Eq.(19) is better for larger-size pipes or regular-geometry conduits, where the local void fraction normally experiences a sharp increase at a short distance from the wall as compared to the conduit lateral dimension (Lucas and Tomiyama, 2011). If the relative distance from the wall increases, such as in narrow conduits, the effective gas flow gets reduced, the average gas velocity increases, and the average void fraction decreases. This, in turn, is de-facto equivalent to a reduction in the average drag coefficient.

As can be readily shown, differences between the drag coefficient for spherical and distorted bubbles of a comparable size are quite significant. Furthermore, within each category, using different formulae available in the literature yields different results, which reflects the fact that significant uncertainties are always present in the evaluation of drag force. The associated modeling uncertainties get augmented in flow situations which involve spacer-induced bubble breakup. Thus, to capture the first-order phenomena reflecting the impact of drag force on phase distribution, and to filter out secondary factors at the model-tuning level, it is important to that observations given above be appropriately used to formulate a model consistent with the dominant flow characteristics.

3.3. Virtual Mass Force

The virtual mass force accounts for the acceleration-induced resistance exerted on dispersed particles by the surrounding fluid. An analytically derived expression for this force is given by Drew et al. (1979)

$$M_{l \rightarrow v, k}^{VM} = -C_{VM} \alpha_k \rho_l \left(\frac{D\bar{u}_{v, k}}{Dt} - \frac{D\bar{u}_l}{Dt} \right) \quad (21)$$

where C_{VM} is the virtual mass coefficient, the standard value of which is 0.5.

3.4. Turbulent Dispersion Force

The turbulent dispersion force represents the force on the gas field caused by turbulence-induced fluctuations of liquid velocity. Podowski (2009) has derived the following form of the turbulent dispersion force

$$M_{l \rightarrow v, k}^{TD} = \alpha_{v, k} \rho_l \nabla \cdot \left[(1 - \alpha) \overline{u_l'^2} \right] \quad (22)$$

where u_l' is the lateral component of the fluctuating liquid velocity, normal to the conduit wall. Since turbulence in both single-phase and two-phase flows experiences a significant degree of anisotropy, it turns out that whereas the lateral turbulent kinetic energy distribution is normally highly non-uniform the average lateral velocity fluctuations are nearly uniform (Wang et al., 1987). Thus, as long as RANS turbulence models are used in computer simulations, Eq.(22) can be replaced by (Podowski, 2019)

$$M_{l-v,k}^{TD} = -C_{TD} \alpha_{v,k} \rho_l k_p \nabla \alpha \quad (23)$$

where $C_{TD} = \frac{\overline{v_{l,p}^2}}{\kappa_p} < 1$ is the turbulence-dispersion force coefficient and the index, p , represents the near-wall locations of the corresponding variables. Based on the experimental data (Wang et al., 1987), a value, $C_{TD} \approx 0.5$, can be used.

3.5. Lift Force

The lift force is due to the combined effects of a non-uniform local velocity distribution around individual bubbles (a Bernoulli-type effect), combined with the bubble-to-liquid relative velocity. The first-principle analytical expression derived for this force exerted on small spherical bubbles is

$$M_{l-v,k}^L = -C_L \alpha_{v,k} \rho_l \bar{u}_{r,k} \times (\nabla \times \bar{u}_l) \quad (24)$$

where C_L is the lift coefficient and the negative sign reflects the fact that the force is directed along a decreasing liquid velocity.

A theoretical value of the lift coefficient for the inviscid laminar liquid flow around a single spherical bubble is 0.5. For viscous fluids, the experimental data and DNS simulations for dilute flows and spherical bubbles show a wide range of values of this coefficient, from 0.01 to 0.3 or even higher (Eichorn and Small, 1964; Tomiyama et al., 2002; Feng and Bolotnov, 2017).

Because different sources of reference may show dramatically different values of C_L for any given flow conditions, and the fact that most data refer to laminar or nearly-laminar flows, their use for the modeling of turbulent flows is not practical. A more consistent first-principle approach to turbulent flows in long conduits is based on the lateral force balance principle. Jiao and Podowski (2012) used the experimental data of Wang et al. (1987) and showed that a reasonable choice of lift coefficient is between 0.02 and 0.04, and $C_L = 0.03$ matched best the measured void fraction and liquid velocity distributions. This result confirms the values used before by Kurul et al. (1996) and Alajbegovic et al. (1996) for both adiabatic and diabatic two-phase flows.

It is interesting to notice that equalizing the expressions given by Eq.(23) and Eq.(24) implies that the results of model's predictions mainly depend on the ratio, C_L/C_{TD} , rather than independently on each individual coefficient. Using the values given above, i.e, $C_{TD} = 0.5$ and $C_L = 0.03$, the ratio of the lift-to-'turbulent dispersion' coefficients for spherical bubbles becomes, $C_L/C_{TD} = 0.06$. Whereas the above observation facilitates model validation at fully-developed flow conditions, it also indicates that even a well-calibrated model at such conditions will not necessarily properly predict details of developing flows in which the lateral liquid velocity may affect both coefficients.

It has been well-documented experimentally by Lucas and Tomiyama (2011), and also confirmed by computer simulations (Feng and Bolotnov, 2017; Ervin and Tryggvason, 1997), that when a bubble becomes distorted from spherical shape, the lift force changes direction, so that large bubbles are normally pushed toward the center of a conduit and that the sign of the lateral void fraction gradient gets reversed. Attempts have been made to either estimate the corresponding threshold bubble size (Kurul and Podowski, 1988) or to quantify it in the form of correlations (Tomiyama et al., 2002) but such results are typically limited to a specific range of experimental conditions of reference. Accurate predictions over a broad range of conditions are

extremely difficult due to the fact that the critical bubble diameter depends not only on the gas and liquid volumetric fluxes but is also affected by the conduit size. The latter effect has been clearly demonstrated by Lucas and Tomiyama (2011). Their experiments performed for relatively low gas-to-liquid superficial velocity ratios in a 200 mm diameter pipe indicate a sign change in the lift coefficient for bubbles of about 6 mm diameter, whereas the critical size gets reduced to below 5 mm for flows in a 50 mm pipe.

The available experimental evidence indicates that the lift coefficient sign change is quite abrupt. Whereas the experimentally-deduced values after the change cover a broad range, it should be recognized that a small change of bubble size around the threshold value will likely have a small effect on the turbulence dispersion force. Thus, in the case of well-established turbulent flows, a consistent approach is to use again the lateral force balance and, thus, the same magnitude of the lift-to-‘turbulence dispersion’ coefficients ratio for both cases.

3.6. Single Bubble-Group Two-Field Model

Given the uncertainties associated with both the closure laws for the interfacial forces and the RANS-level model of turbulence in gas/liquid two-phase flows, using a simplified two-field model may serve as a useful tool allowing for capturing dominant phenomena governing flow and phase distributions while filtering out secondary factors at the model-tuning level. However, it is important that the applicability of such model be properly understood for different flow conditions, as demonstrated below.

Summing up the mass and momentum conservation equations for individual bubble size groups, Eq.(8) and Eq.(10), respectively yield

$$\frac{\partial \alpha}{\partial t} + \nabla \square \sum_{k=1}^K (\alpha_{v,k} \bar{u}_{v,k}) = 0 \quad (25)$$

$$\rho_v \left[\frac{\partial}{\partial t} \sum_{k=1}^K (\alpha_{v,k} \bar{u}_{v,k}) + \nabla \square \sum_{k=1}^K (\alpha_{v,k} \bar{u}_{v,k} \bar{u}_{v,k}) \right] = -\alpha \nabla P + \alpha \nabla \square \left[\underline{\underline{\tau}}^{tot} \right] + \alpha \rho_v \bar{g} + \bar{M}_{l-v}^i \quad (26)$$

Introducing the averaged gas velocity defined as

$$\bar{u}_v = \frac{1}{\alpha} \sum_{k=1}^k (\alpha_{v,k} \bar{u}_{v,k}) \quad (27)$$

and assuming that

$$\sum_{k=1}^k (\alpha_{v,k} \bar{u}_{v,k} \bar{u}_{v,k}) \approx \alpha \bar{u}_v \bar{u}_v \quad (28)$$

Eq.(27) and Eq.(28), respectively, can be rewritten as

$$\frac{\partial \alpha}{\partial t} + \alpha_v \bar{u}_v = 0 \quad (29)$$

$$\rho_v \left[\frac{\partial}{\partial t} (\alpha_v \bar{u}_v) + \nabla \square (\alpha_v \bar{u}_v \bar{u}_v) \right] = -\alpha \nabla P + \alpha \nabla \square \left[\underline{\underline{\tau}}^{tot} \right] + \alpha \rho_v \bar{g} + \bar{M}_{l-v}^i \quad (30)$$

The combined Eq.(7), Eq.(9) and Eqs.(29)-(30) assume the form of a two-field model. However, when considering the application of such a model to a flow of poly-dispersed spherical bubbles, one should realize that the interfacial force terms in Eq.(9) and Eq.(30) are actually nonlinear combinations of state variables for the individual groups, such as velocities and

volumetric concentrations. Naturally, the same observation applies to Eq. (28). So, as long as the bubble sizes, and thus velocities, are considerably different from one group to another, a single-group two fluid model may be unable to properly reflect some of the important flow characteristics (such as void distribution).

On the other hand, when the majority of bubbles of different group sizes are in the deformed-shape range, while their volumetric fractions remain small, it can be shown (Podowski, 2018) that the relative velocities and, thus, the absolute local velocities of all bubble groups will be approximately the same. Thus, the set of equations given by Eq.(7), Eq.(9), Eq.(18), Eq.(21), Eq.(23), Eq.(24) and Eqs.(29)-(30) can be interpreted as a consistent two-fluid model of a two-phase flow of multiple-size deformed (or ‘large’) bubbles. The major factor critical for the accuracy of the simplified model is the fact that for small void fractions we have:

$$C_{D,k} / d_{b,k} \approx \text{constant for } k=1,2,\dots,K.$$

4. Computational Modeling

4.1. CFD Solver

The two-phase flow model discussed in the previous sections has been implemented in the Computational Multiphase Fluid Dynamics (CMFD) code, NPHASE-CMFD (Antal et al, 2000). NPHASE-CMFD is a RANS-level, pressure-based finite-volume parallel processing solver capable of tracking individual components of multiphase multicomponent fluids capable of analyzing unsteady and steady flows. It employs the multi-field modeling concept to solve the conservation of mass, momentum, and energy equations, combined with the corresponding interfacial jump conditions, for each component fluid. The mass and momentum equations are solved using a coupled solver providing additional robustness necessary to achieve convergence in the complex rod bundle with spacers. The code also includes the transport equations for turbulence quantities and chemical species. The code is fully unstructured and includes second-order accurate convection and diffusion discretization. Phasic and field conservation equations are solved in coupled or segregated fashions, using frozen coefficient linearization. One of several discrete integration methods can be used, including the upwind, hybrid and second order upwind schemes. The modeling capabilities of the NPHASE-CMFD solver have previously been extensively validated against experimental data (Tiwari et al., 2006; Shaver and Podowski, 2015). The experience gained from those studies indicates that, due to the complexity of two- and multiphase flows, the choice of best solution method may vary with problem characteristics. Based on preliminary parametric testing, the hybrid method has been used in the present work.

4.2. Computational Domains and Grid-Size Studies

The formulation and testing of the computational mesh for the present analysis capitalized on the extensive past experience at the RPI Center of Multiphase Research with numerical simulations of multiphase flows for a broad range of geometries and operating conditions, including flow and phase distribution in fuel assemblies with spacers of different geometries (Anglart et al., 1997, Antal et al., 2001) and in conduits with elbows and bends (Tiwari et al., 2006; Telishcheva et al., 2010), conduits experiencing local gas injection (Bolotnov et al., 2012; Behafarid et al., 2013) and flow along sudden contractions, expansions and other obstructions (Waite et al., 2012; Kurul and Podowski, 1996; Antal et al., 1998; Gallaway et al. 2007). When combined with the results of investigations of major generic conceptual issues arising from the modeling of gas/liquid two-phase flows at the RANS level (Podowski, 2009, 2019a; 2019b;

Podowski and Shaver, 2013; Shaver et al., 2013; Shaver and Podowski, 2015), they can be summarized as follows:

- The effect of dispersed bubbles near solid walls on local liquid velocity field limits the applicability of Low-Reynolds Number k - ϵ model and other similar RANS models highly questionable or even not applicable at all.
- Standard conditions used by the High Reynolds Number (HRN) k - ϵ model yield a mesh configuration which is consistent with the ensemble-averaging principle over a large range of bubble sizes.
- The acceptable range of the near-wall grid size (y_p^+) is typically between 30 and about 200, including both straight and curved conduit walls, as well as insert tips and the associated sudden flow obstructions.
- It is not uncommon that reducing the grid size beyond the limits imposed by the presence of bubbles may adversely affects the accuracy of in two-phase flow RANS simulations.
- The trend mentioned above is not only due to the modeling of turbulence but is also associated with the modeling of spatially-averaged bubble-liquid interfacial interactions (mass, momentum and energy exchange).

The computational domain for CFD simulations has been built using dimensions from the SUBFLOW experiment (Ylönen, 2013). The rod bundle with mixing-vanes offers a unique challenge as the mesh requires a sufficiently large number of elements to capture the detailed governing phenomena, but the problem still needs to be solved efficiently and accurately. In the current case, the mesh was generated using Pointwise V16.04 (Pointwise, 2011), ensuring that there are structured boundary layers on the wall surfaces which include the spacer and the rod walls. The region around the mixing vanes uses unstructured tetrahedral elements in order to fill in the mesh points where the geometry is most complicated. All other regions use prisms or hexahedral elements to compose the radial topology. The resultant topology is shown in Figure 7(a) and (b) with an example cutaway into the mesh around the vanes for a single channel in Figure 7(c). This topology has been kept the same before and after the spacer grid, to allow for the locations downstream to be set as the inlet if necessary. This allows for performing the calculations for the experimental case without spacers, the results of which can be used as the inlet to the spacer grid cases. This assumption is consistent with the experimental method, and it allows one to create a full picture of the flow conditions for each case. In this work, the steady-state solver has been used with false-time stepping to achieve satisfactory convergence. Each run continued for at least 4000 iterations which allowed the root mean squared residuals to be between 10^{-7} and 10^{-5} for u , v , w , slightly above 10^{-5} for α , and 10^{-3} for P .

Major dimensions of a single sub-channel contained in the 16 channel bundle are shown Figure 7(d). Whereas the geometry has been scaled up by a factor of 2.6 from a typical PWR, there are still some local flow paths as small as 3-5 mm where larger bubbles may get slightly distorted. However, details in this regard are beyond the resolution level of both the experiment and the modeling framework. As shown in Figure 1(a), the split-type mixing-vanes use an alternate orientation which provides swirling within each subchannel as well as cross flow between the neighboring subchannels. The interior surface comprising the spacer grid has been formulated using a thin-wall assumption. However, the effect of thickness of spacer plates on the results of predictions has been examined in a separate study (Waite et al., 2014, Waite, 2018) and found to be practically negligible. This is due to the fact that the only effect of spacer thickness captured is on the local pressure loss due to a slight flow area reduction, but it has been shown to

be very small compared to that of the mixing-vanes geometry (Chun and Oh, 1998). All walls treat the liquid phase as no-slip boundaries. The inlet condition is an inflow conditions and the outlet condition is a relative pressure condition. So, the current setup allows for properly capturing local swirling and cross-flows in the rod bundle.

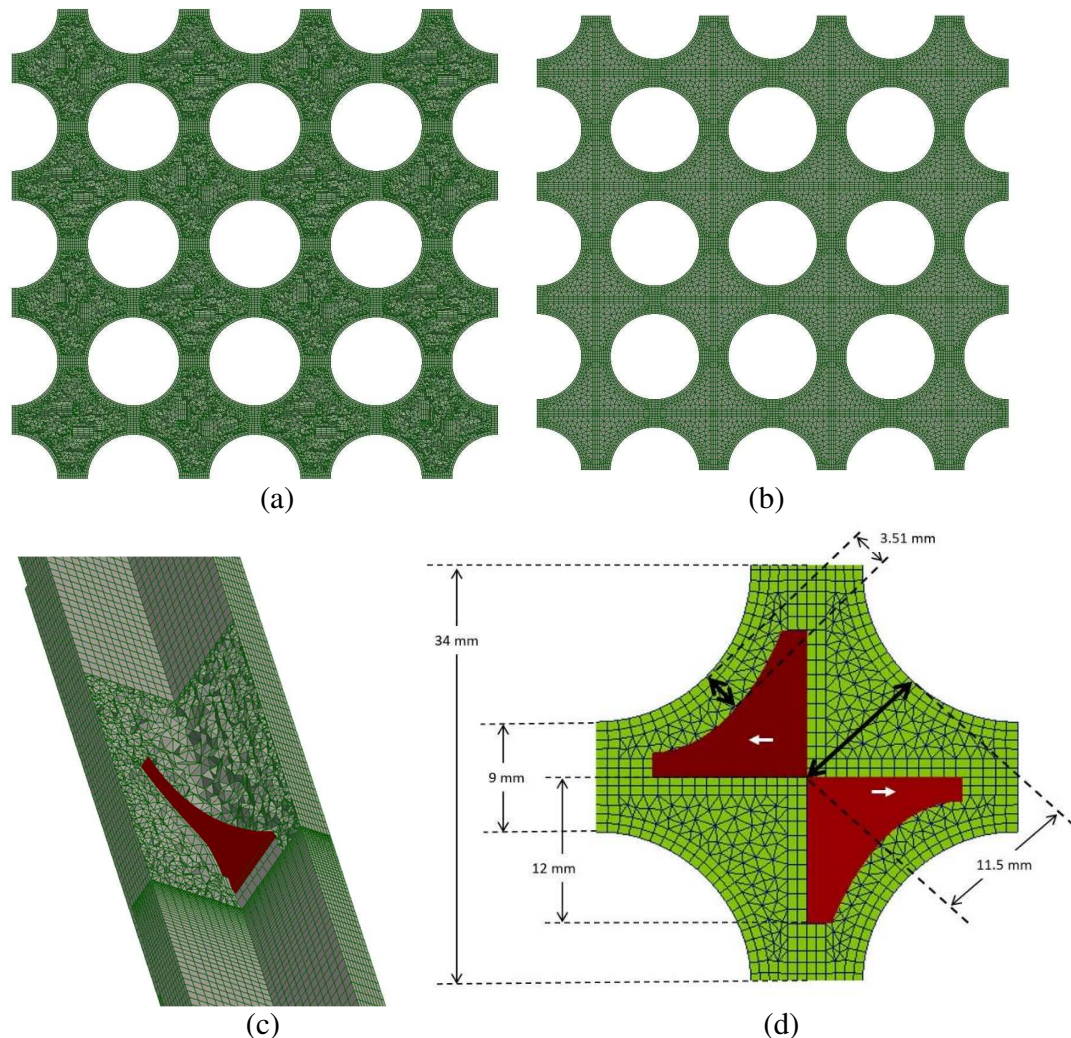


Figure 7. Grid topology of the rod bundle (a) within vanes, (b) before and after spacer region, (c) 3-D view of grid details in the spacer region, (d) projected grid around mixing vane fins.

The sensitivity of the computational results to the mesh size and shape needs to be explored in every computational study. Therefore, four different grids of varying characteristics were analyzed to ensure that the results were consistent across the different grid set ups. The grid study has been performed for a 2 x 2 rod bundle without spacers. The differences of each grid can be seen in Table 2 and in Figure 8. The importance of this study is augmented by the fact that the wall structures are close together, making it difficult for the structured boundary layers to always satisfy the near-wall node size requirements. The results shown in Figure 9 confirm the consistency of the grid structure used for the experimental comparisons (Case 2). As can be seen in Figure 9(a), the axial pressure drop for all the grids is the same. The radial plots in Figure 9(b) and (c), indicate that the absolute differences in the local void fraction do not exceed 0.003 and the maximum velocity differences do not exceed 0.02 m/s. Thus, one concludes that the results of

simulations discussed in this paper are practically grid-independent. Interestingly, the corresponding relative errors, especially in the central flow regions, are below 3-4% for void fraction and 2-3% for velocity. Needless to say, they are well within the predictive accuracy of the physical models used in the analysis.

Table 2. Grid Study Differences

| Case # | y+ | Structured Boundary Layer In Rod Gap? | Elements |
|--------|-------|---------------------------------------|-----------|
| 1 | 20-25 | Yes | 1,561,600 |
| 2 | 14-18 | Yes | 2,745,600 |
| 3 | 14-18 | No | 2,534,400 |
| 4 | 29-34 | No | 864,000 |

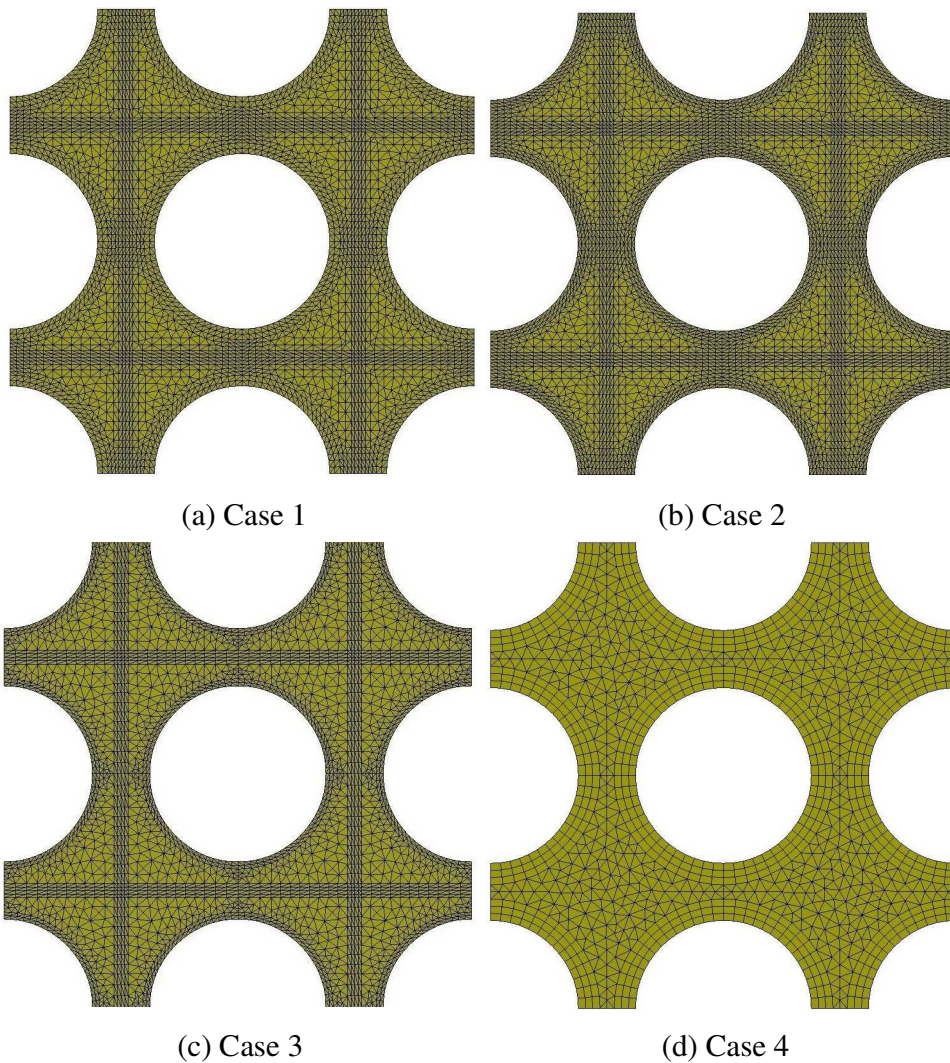


Figure 8. Topology of the four grids used in parametric testing of mesh impact on the results of NPHASE-CMFD simulations.

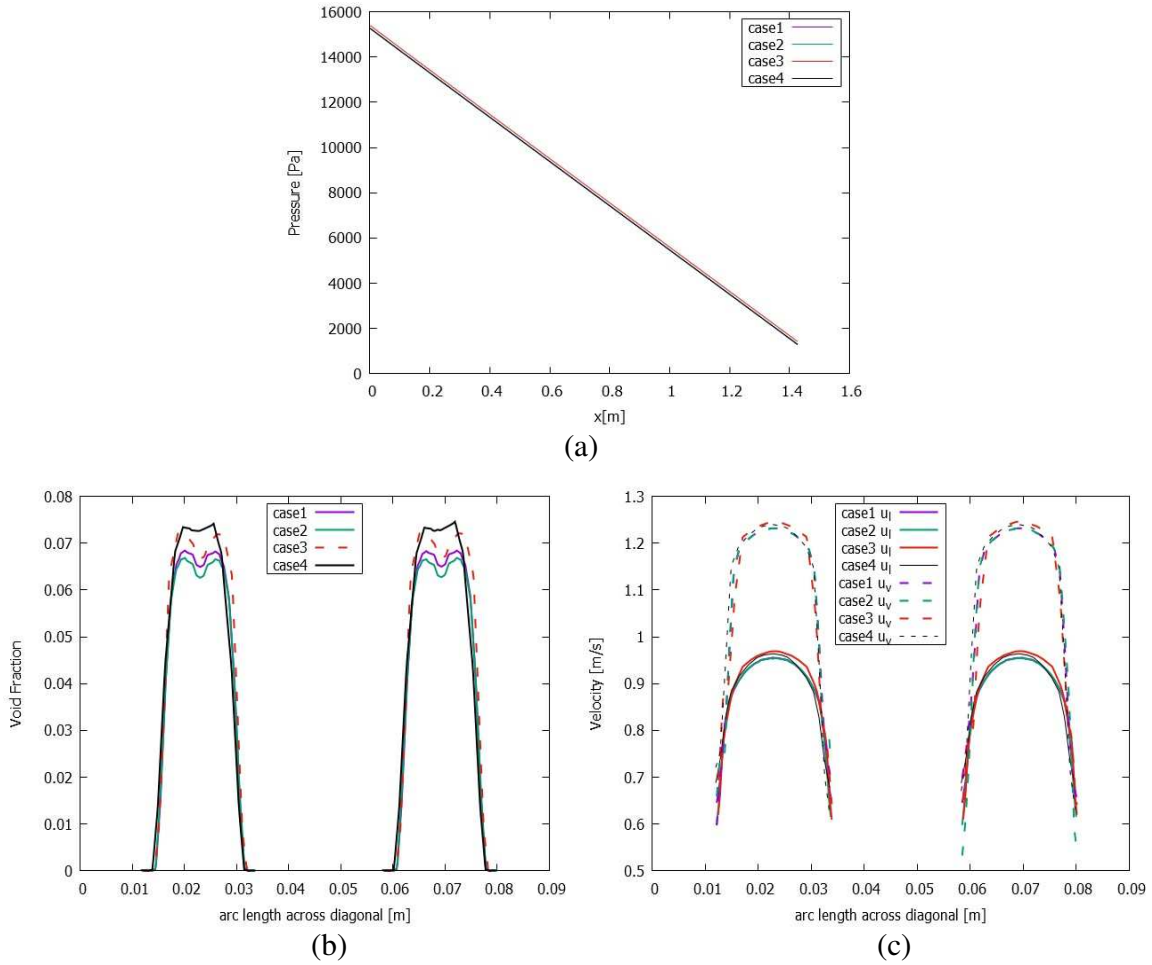


Figure 9. Results of the grid study: (a) axial pressure drop, (b) lateral void fraction across diagonal, (c) axial velocity across diagonal.

Since the modeling of turbulence at the RANS level in complex geometries of reactor fuel assemblies is a challenging issue, it has been studied extensively before. Liu et al. (2012) investigated single-phase flow downstream of mixing vanes using six different turbulence models. Yuan et al. (2013) looked at the accuracy of three different turbulence models using two different computer codes. Cinosi et al. (2014) benchmarked three turbulence models using the MATIS-H experimental data downstream from mixing vanes. A general conclusion from the above studies has been that whereas the inherent averaging concept behind standard $k-\epsilon$ models does not allow for tracking details of the fluctuating components of turbulence, such models are capable of capturing not just the bulk flow, but also cross flows and heat transfer enhancement. A similar conclusion has also been drawn by Chen et al. (2017) based on mixing-vane rod bundle studies.

Interestingly, it has also been shown by Podowski and Shaver (2013) (also, see (Podowski, 2019)) that the combined HRN $k-\epsilon$ and bubble-induced turbulence model in two-phase flows properly predicts the lateral void and velocity drifts between the subchannels in heated reactor fuel assemblies. A similar turbulence model has been used in current study. Figure 10 shows the predicted void fraction profiles with lateral liquid velocity vectors in the upper left quadrant of the rod-bundle for the SUBFLOW experimental conditions corresponding to Case 1-3 in Table 1. The velocity vectors at the tip of the mixing vane (Figure 10(a)) show an interesting detail captured by the simulations. Specifically, it can be seen that large vortices are created by the

mixing vanes, whereas small vortices are also formed at the “knee” of the mixing vane in the outer areas of a channel, which is where the curved surface starts at the bottom of the vane. The alternating vane pattern is also clearly seen in this result, as the strong lateral velocities in each channel are rotated 90° from its neighboring channels. At a distance of 50 mm downstream from the vane (seen in Figure 10(b)) some of the smaller structures have already decayed, but there are still strong vortices visible in the center of the channels around high void concentration regions. The bottom left channel is located in the middle of the bundle and it experiences more cross flow, which causes the void to spread out. It is important to notice that this velocity behavior is similar to the flow structure reported by Chang et al. (2008).

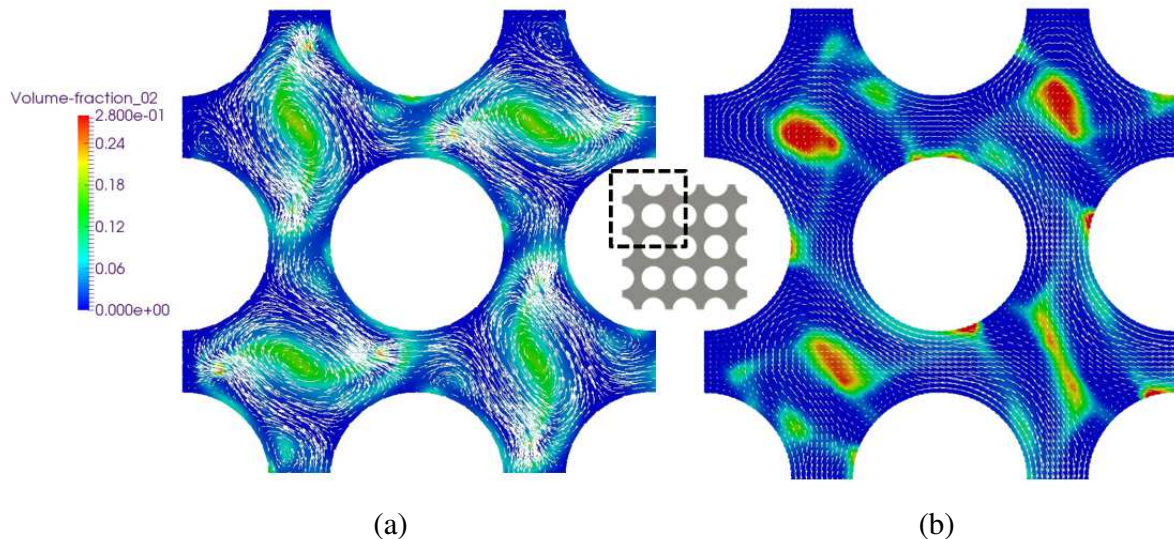


Figure 10. Predicted Case 1-3 void fraction (color contours) with lateral liquid velocity vectors overlaid in the upper left quadrant of the 16 channel bundle: (a) at the tip of the mixing vanes, (b) 50 mm downstream.

5. Analysis of Coupled Experimental and Theoretical Results

Two cases, each representing a different gas flow fraction and a different bubble diameter, have been used in this study to show a comparison between the experimental results based on two methods of data reduction and the results of NPHASE-CMFD simulations using the model discussed in Section 4. These cases are: Case 1-1 and Case 1-3 in Table 1. Case-1 pertains to a small gas superficial velocity and small spherical bubbles. On the other hand, the bubble sizes in Case 1-3 are predominantly in the deformed bubble-shape flow range and the gas volumetric flow rate fraction is higher than that in Case 1-1, although still quite low. For both cases, a thorough analysis of the experimental results has been performed using two data reduction methods, and the bubble size distribution has been determined for the experiments with and without spacer grids.

5.1. Small Bubbles- Case 1-1

The experimentally-estimated bubble size distribution for Case 1-1, based on the signals captured by the wire mesh, is shown in Figure 11. As can be seen, the maximum void fraction of about 0.8% corresponds to the bubble diameter of 3.5 mm, whereas the average bubble size has been estimated at 3.72 mm, both below the threshold limit for bubble deformation. The small gas flowrate led to a small size standard deviation of 0.62 mm. The vanishing of the weak local

maximum at a bubble diameter of 4 mm and the tendency to move the left slope towards lower bubble diameters are hints for a slight bubble breakup effect. With a growing distance from the spacer, the distribution tends to return gradually to the unperturbed one, which is dominated by small bubbles.

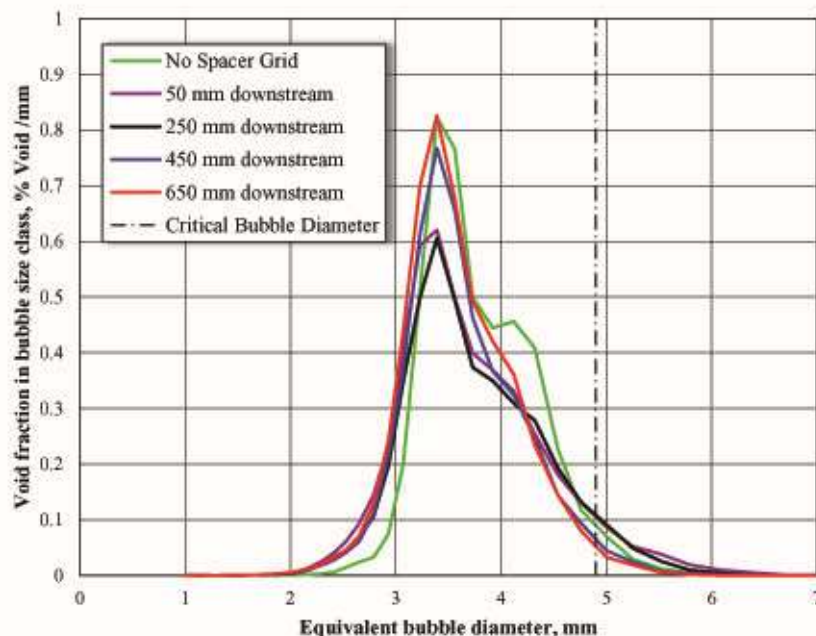


Figure 11. Case 1-1: Effect of bubble-size on the void fraction.

The fact that the majority of the bubble population corresponded to a narrow 3-4 mm diameter range indicated that a two-fluid model discussed in Section 3 should be capable of reproducing the experimental data. The calculations have been performed using the experimentally determined average bubble diameter (3.72 mm), with the drag coefficient given by Eq.(16) and the lift coefficient of 0.03.

The first objective of the analysis has been to evaluate the flow conditions which are comparable to the experiment without spacers. As can be seen in Figure 12, the void fraction distribution observed in the NPHASE-CMFD simulation is in good agreement with the behavior shown by the experimental data. The void fraction in simulations and the experiment hug the walls, which is typical of small bubbles. The experimental results, which include two methods of data processing, “Linear cut” (Ylönen, 2013) and “Maxwell no cut” (Prasser and Haefeli, 2018), show the concentrations for the “Maxwell no cut” are lower. The experimental results show that the measured bubble concentration around the rods is somewhat non-uniform in the azimuthal direction. This is likely due to the inherent random asymmetries in the distribution of bubbles leaving centrally-located air injectors in each channel. Since a uniform inlet void distribution has been assumed in the simulation, the calculated void fraction distribution at the sensor location is nearly uniform among the neighboring channels, as expected. However, the overall behavior is similar in both cases, consistent with the underlying physics. It is also interesting to notice that the bundle-averaged void fraction shown in Figure 6 agrees well with the measured value.

The plots and data points across the diagonals of the rod bundle are shown in Figure 13. They indicate that the magnitude of the wall peaks is captured well by the NPHASE-CMFD-based model. There are differences seen in the centers of the channels where the calculated void fraction is nearly symmetrical around the maximum velocity lines, whereas the measured values

experience small random asymmetries. The calculated central-peak void values of the order of 0.001 to 0.002 reflect the left-over bubbles expelled from the completely depleted narrow passages between the rods, and the fact that the lift force drops to zero at the locations of maximum velocity. At the same time, since the average void fraction is less than 0.005, the experimental data reflect the randomness of void distribution. A comparison between the two methods of data processing shows that they yield similar results at locations where the void fraction experiences small lateral changes, but may be different from each other at steep void fraction increases near rod surfaces. Thus, using both methods provides a useful insight into the proper interpretation of the measurements, although the “Maxwell No Cut” method is more accurate. The overall results confirm the consistency of the model in terms of preserving the diagonally-averaged gas volume. Furthermore, the peak void fractions in the diagonally-peripheral subchannels seem to be slightly lower than in the central channels, but the differences are practically within the experimental and modeling uncertainties . discussed in Section 2 and Section 4, respectively.

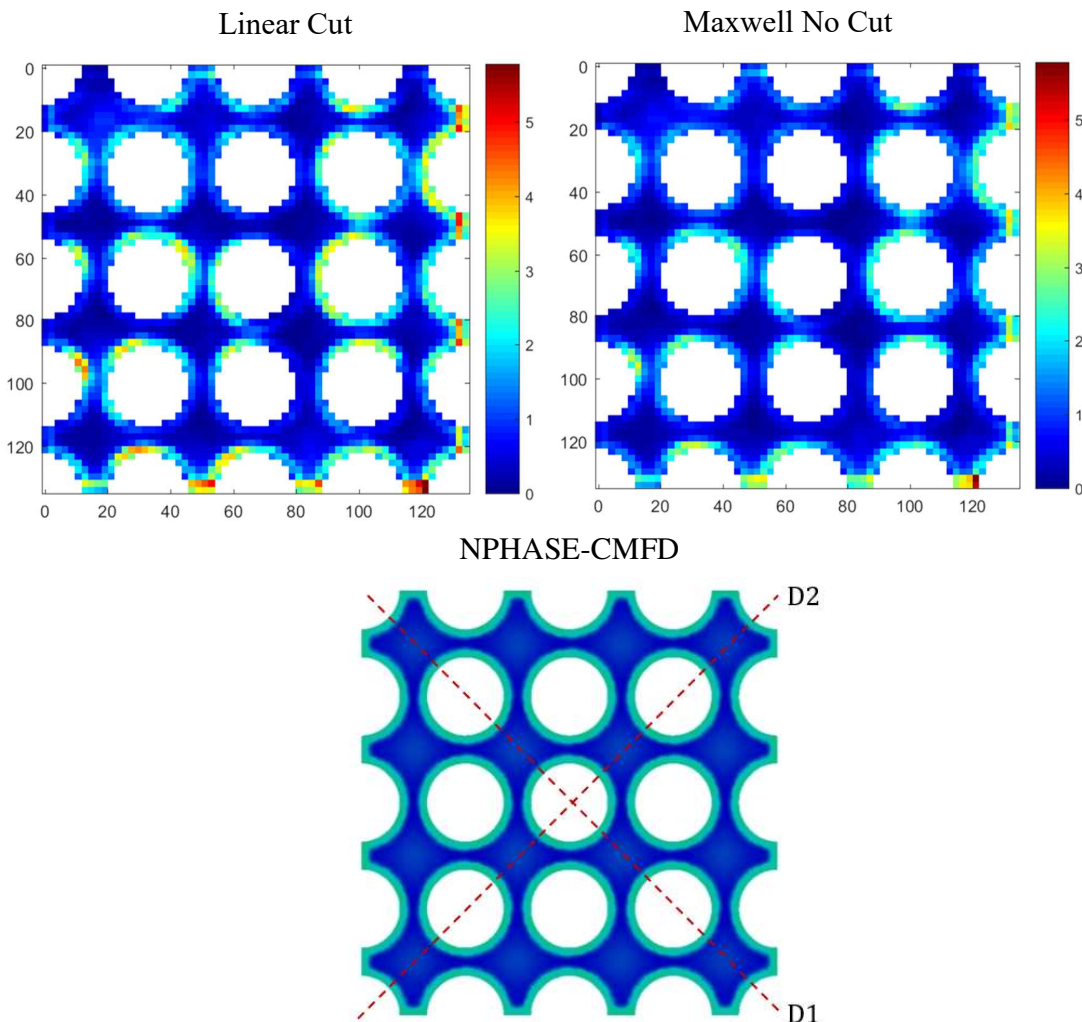


Figure 12. Case 1-1: Color contours of local void fraction distribution with no spacer. The experimental color contours have been generated using both the “Linear Cut” and the “Maxwell

“No Cut” methods of data processing. (The experimental and theoretical color contours have been generated using identical color scales, length units are mm)

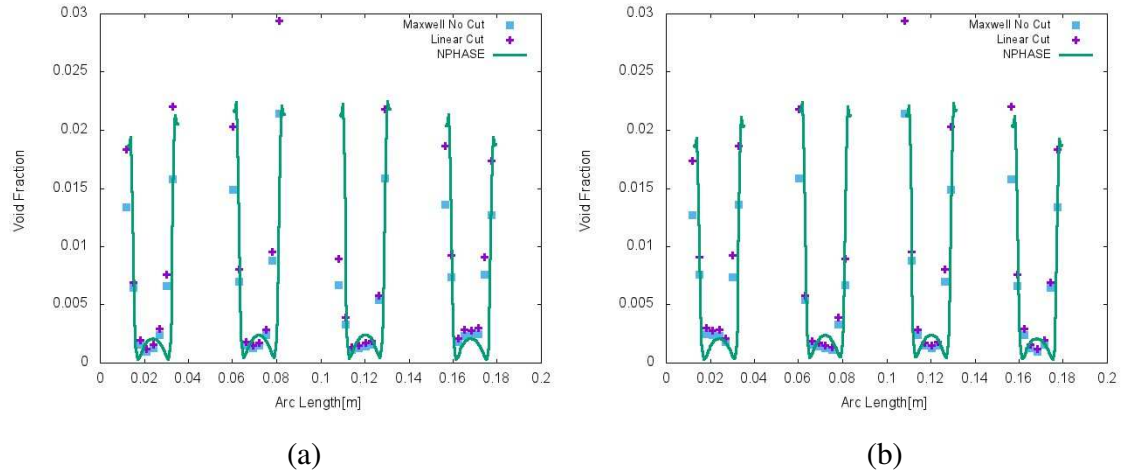


Figure 13. Case 1-1: Void fraction distribution along diagonals with no spacer: (a) diagonal D1, (b) diagonal D2 (see Figure 10 for a location reference).

The NPHASE-CMFD results without spacers have then been used as the inlet conditions to the simulation with spacers. This is consistent with the experimental conditions just upstream from the spacer. The experimental and predicted void distributions downstream from the spacer grid are shown in Figures 14, 15, and 16.

The experimental and calculated color contours of void fraction at two locations, 50 mm and 250 mm downstream from the spacer, are given in Figure 14. As can be seen, both the experiment and computation show that the vortices created by the mixing vanes sweep the bubbles away from the fuel rod surfaces toward the center of the channels. This is because bubble distribution at both locations is mainly influenced by the inertial effects associated with the change in momentum imposed by the shape of the vanes. The differences in the magnitude of void peaks between the experiment and simulation are likely caused by the uncertainties in the experimental data analysis and/or due to the limitations of the current models of interfacial forces, in particular in regard to developing two-phase flows. It is evident that capturing detailed effects of the spacer on local bubble shape and distribution is a challenging task faced by both the experiment and the simulation. However, the underlying differences are contained within acceptable limits, so one concludes that the overall behavior observed in the experiment has been properly reproduced by the model.

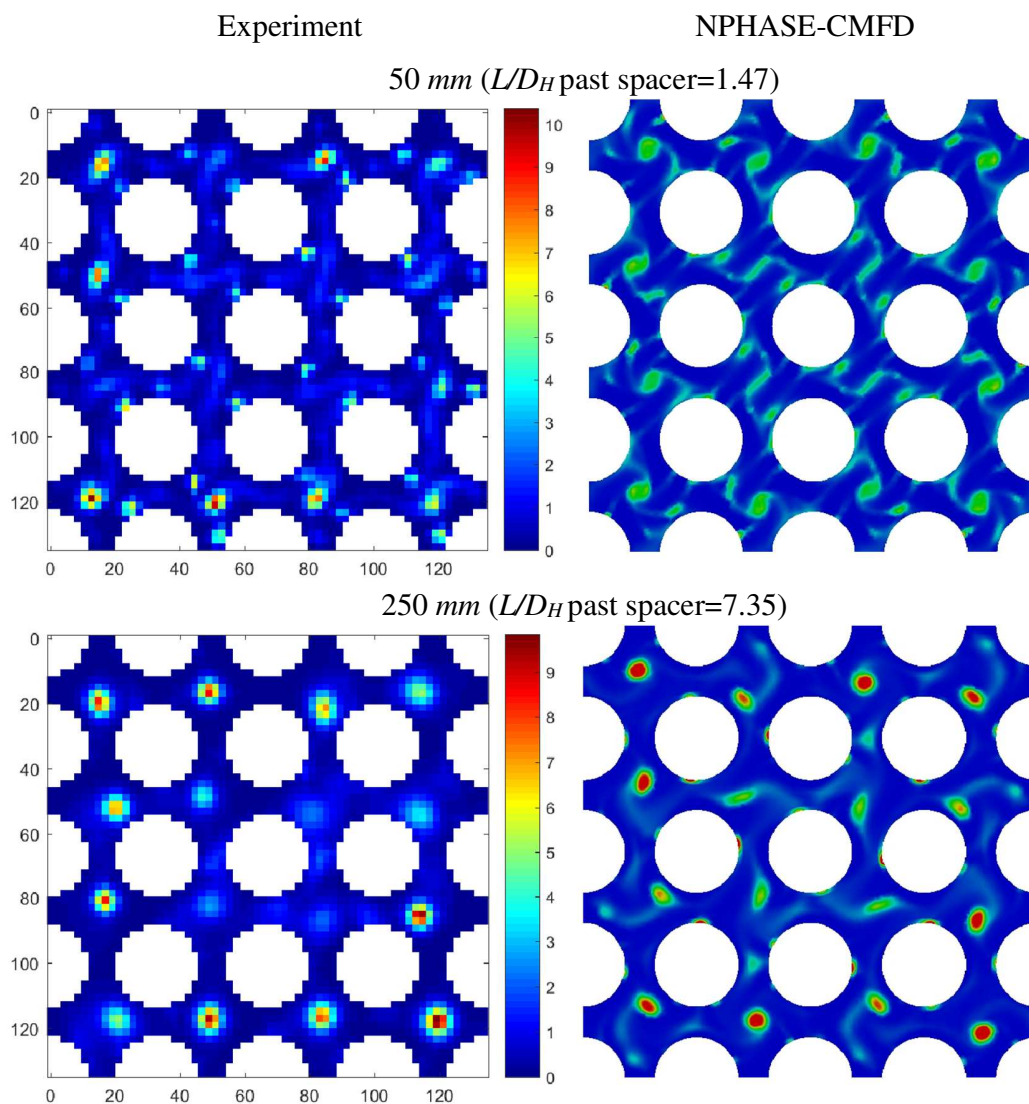


Figure 14. Case 1-1: Void fraction distribution comparison between simulation and experiments with spacer at 50 mm and 250 mm locations downstream from the spacer (scale in percent void). The experimental color contours have been generated using the “Maxwell No Cut” method of data processing (length units are mm).

Figure 15 present the void fraction color contours at 450 mm and 650 mm downstream from the spacer, still for Case 1-1. As the flow moves downstream from $L/D_H = 7.35$ to $L/D_H = 19.12$, the mixing vane effects start to decay, which allows the interfacial momentum forces to redistribute the bubbles. In this region, the uncertainties of the selected bubble size and model

coefficients start playing a larger role. As shown by both the experimental and simulation results, several highest void concentration regions have returned to the fuel rod surfaces 650 mm downstream. This outcome confirms that the flow field is dominated by small bubbles. In both the experiment and the simulation, there are still some voids that remain around the centers of selected subchannels at $L/D_H = 19.12$, with the concentrations being higher in the latter case. However, the trend for the bubbles to be brought into the center and then return to the fuel rod surfaces has been properly captured by the model.

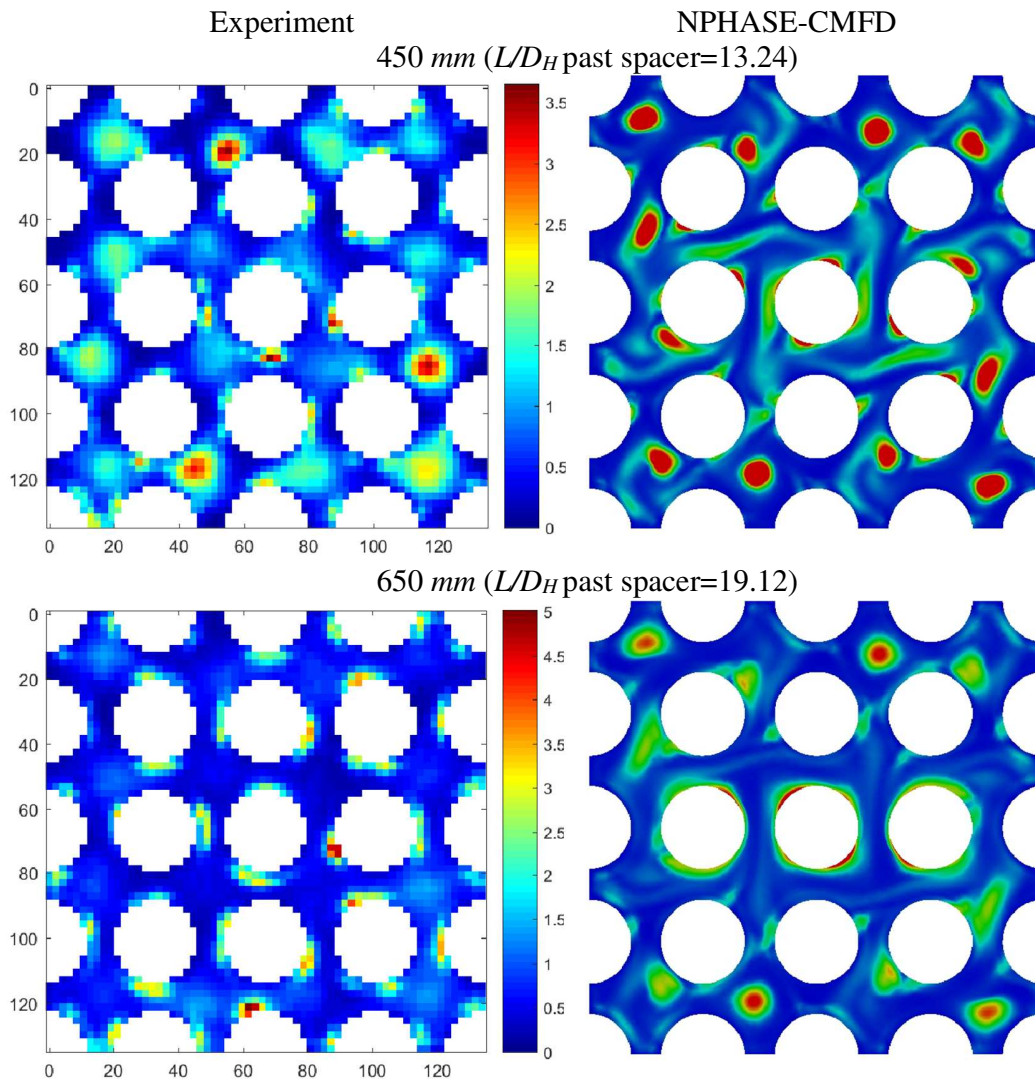


Figure 15. Case 1-1: Void fraction distribution comparison between simulation and experiments with spacer at 450 mm and 650 mm locations downstream from the spacer (scale in percent void). The experimental color contours have been generated using the “Maxwell No Cut” method of data processing (length units are mm).

The void distribution at 650 mm ($L/D_H=19.12$) downstream from the spacer is not as ordered as it was without spacer grids. This is the evidence that this case has not yet returned to the conditions seen upstream of the mixing vanes. As can be seen, the local peaks near the walls in

the simulation are consistent with those seen in the experiments, which gives confidence that the secondary flow directions and magnitudes are being captured accurately well downstream from the spacer grid. However, the more prevalent void peaks in the centers of the outermost channels in the simulations illustrate the difficulties associated with capturing developing flows, which arise from the combined modeling and experimental uncertainties.

The void plots and data points across the diagonals of the rod bundle at a distance of 50 mm downstream from the spacer are shown in Figure 16. Again, the void fraction magnitude between the adjacent rods is captured reasonably well by the model. The calculations also show local near-wall increases along diagonal D1, which have been captured by the experimental plots, and can be clearly seen in the corresponding color images in Figure 14. However, since the void fraction at those locations is less than 2%, it would be difficult to resolve distribution details with a sufficient accuracy using plane cuts across the flow area. Both the experiment and calculation show higher void fraction peaks in the peripheral sub-channels. At the same time, each method of data processing shows unusually high and extremely narrow peaks in the lower and upper left corners, which may be attributed to random factors inherently built in the experimental setup.

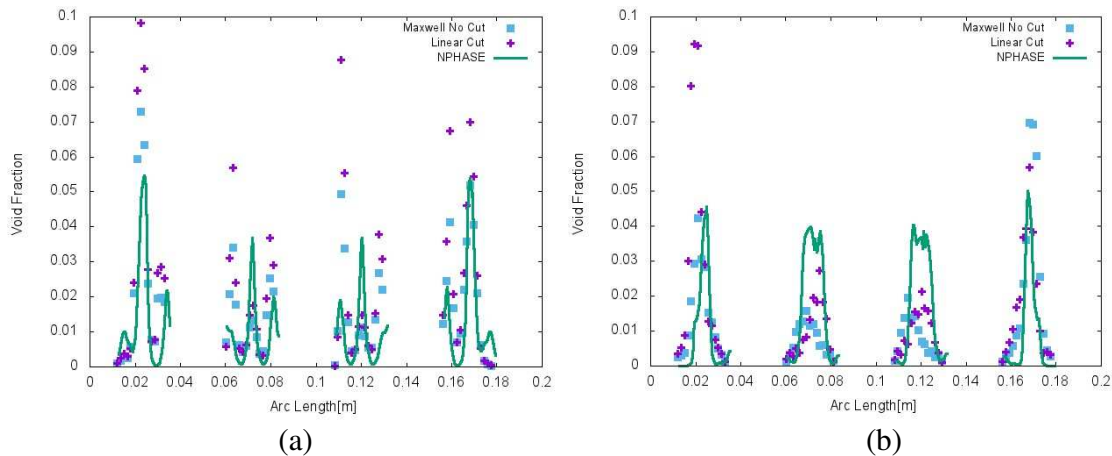


Figure 16. Case 1-1: Void fraction distribution along diagonals 50 mm downstream from the spacer: (a) diagonal D1, (b) diagonal D2 (see Figure 12 for a location reference).

Overall, the qualitative agreement in the behavior of the void fraction between the model predictions and the experimental data at this location is reasonable, although differences can be still be observed in the peak values and locations of sharply changing, while still low, gas concentration across the passages between rods.

5.2. Large Bubbles- Case 1-3

As mentioned before, most bubble sizes in Case 1-3 pertain to the deformed shape range, where the lift force is known to change sign. This observation is confirmed by the cross-section averaged components of the measured void fraction for four different bubble-size ranges, shown in Figure 17, as well as by the corresponding continuous distribution functions of void fraction vs bubble size in Figure 18. The data in both figures refer to the test with no spacer, and to four tests with the spacer, each corresponding to a different location downstream from the spacer.

The void distribution corresponding to four groups of bubble sizes is shown in Figure 19. The grouping scheme reflects the results of experiments of Tomiyama et al. (2002) performed for single bubbles of different shapes in prescribed shear flows. According to those experiments,

the transition in the lift coefficient sign occurred for the equivalent bubble diameters between 4 mm and 7 mm around an estimated value of 5.9 mm. Whereas the current results for the case w/o spacer show a similar trend, it can also be noticed that bubbles of diameters higher than 4.9 mm already depart for the wall and start collecting near the subchannel centers. Such a behavior is consistent with the observations made by Lucas and Tomiyama (2011) in the experiments which were still performed for flows in simple pipe geometries but covered a range of gas concentrations and velocities at actual two-phase flow conditions.

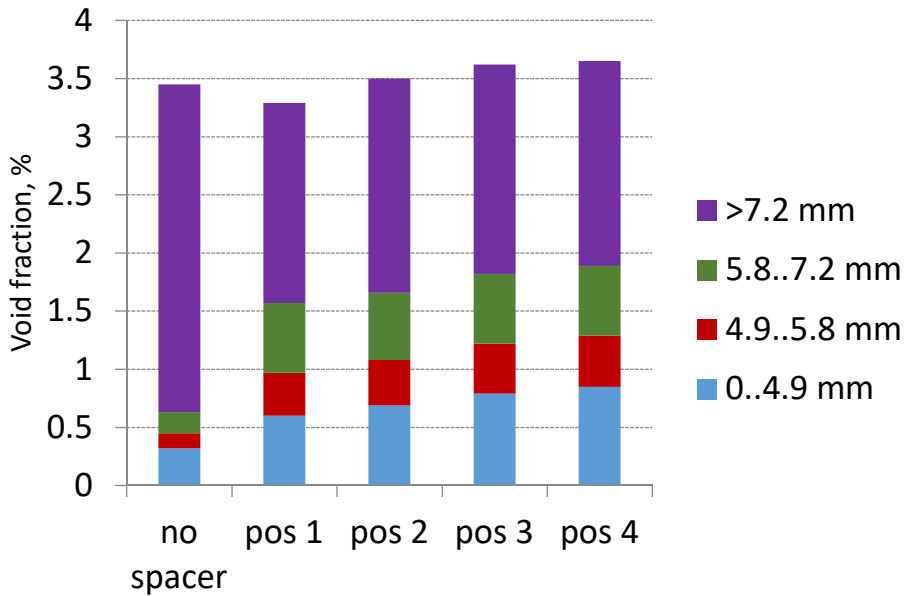


Figure 17. Case 1-3: Cross-section averaged void fraction subdivided into bubble-size ranges. Positions 1, 2, 3 and 4, correspond to the 50 mm, 250 mm, 450 mm and 650 mm downstream from the spacer.

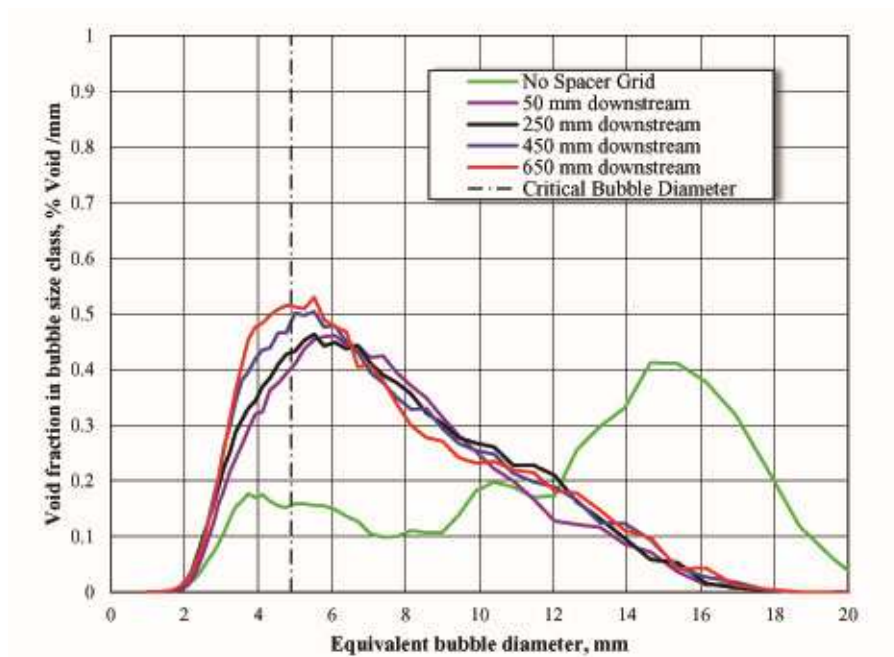


Figure 18. Case 1-3: Effect of bubble-size on the void fraction.

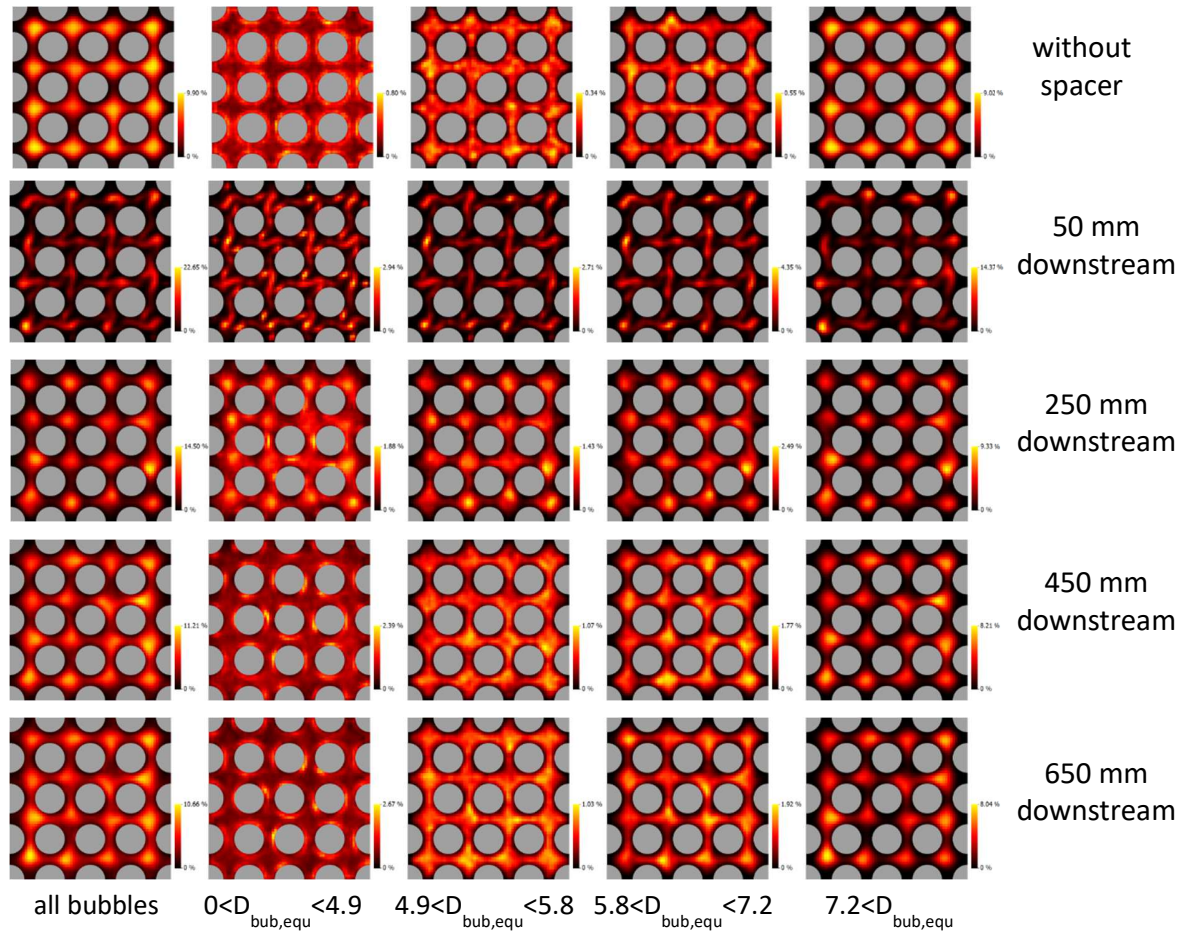


Figure 19. Case 1-3: Total local void fraction and partial volume fractions of bubbles belonging to four different group sizes, at different axial locations relative to the spacer grid.

The color contours of void fraction for the case without a spacer are shown in Figure 20, including the experimental results corresponding to the two methods of data processing discussed in Section 2, and the results of calculations. The calculations have been performed using the experimentally determined average bubble diameter (5.0 mm). The drag coefficient was estimated based on the discussion in Section 3.2 as 0.8, and the lift coefficient was set at -0.03 (Podowski, 2019). As can be seen, the void is center-peaked in both experimental cases, consistent with the bubble sizes (see Figure 18), although the peaks are a little less sharp when using the “Maxwell no cut” method which has been shown to be more accurate.

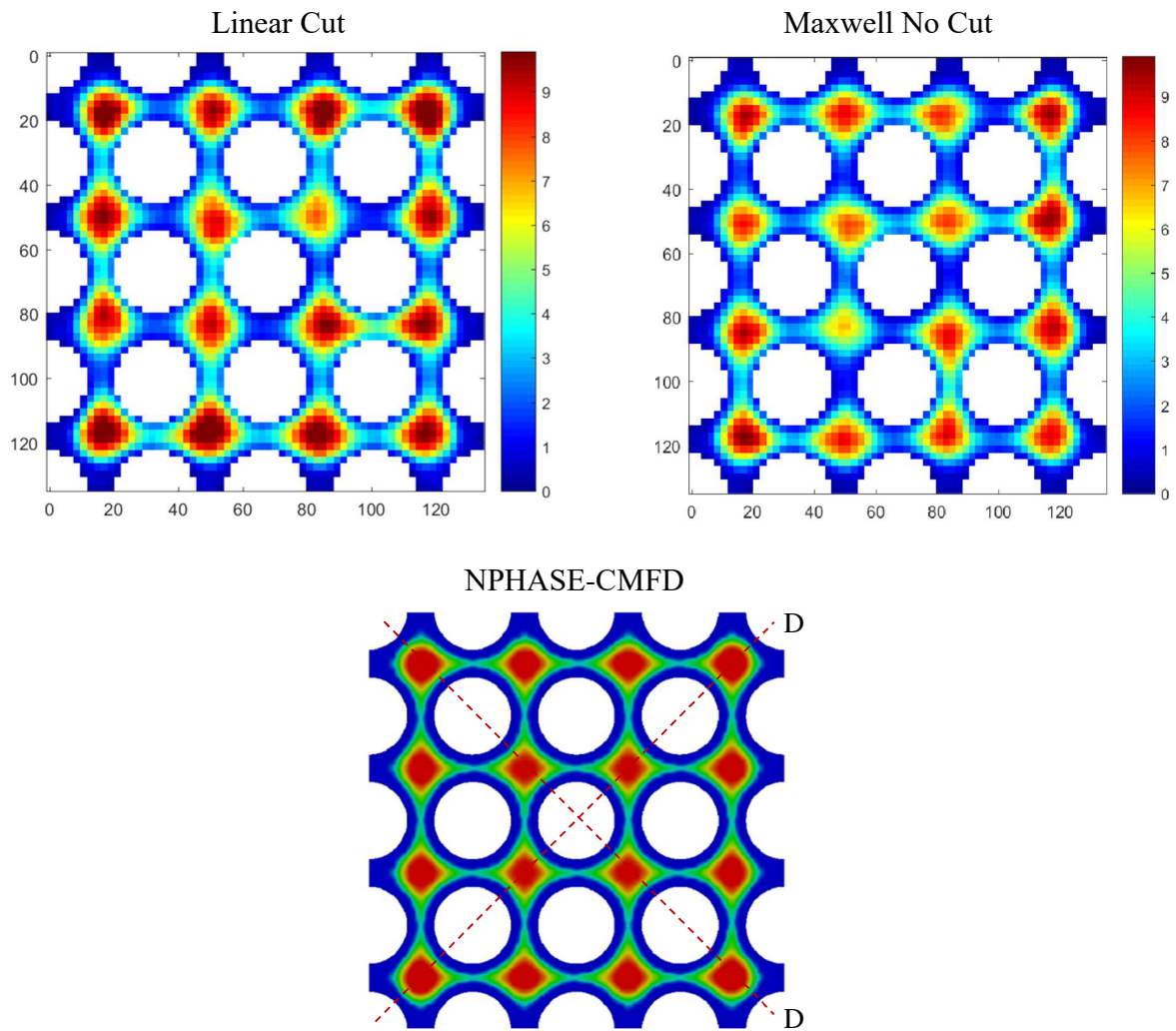


Figure 20. Case 1-3: Color contours of local void fraction distribution with no spacer. The experimental color contours have been generated using both the “linear cut” and the “Maxwell no cut” methods of data processing. (The experimental and theoretical color contours have been generated using identical color scales, length units are mm).

Details of void distribution across two diagonals of the rod assembly shown in Figure 20, are presented in Figure 21. As can be seen, the experimental results show nearly-symmetric void distributions across the individual sub-channels, with higher void peaks occurring in the peripheral subchannels along both diagonals.

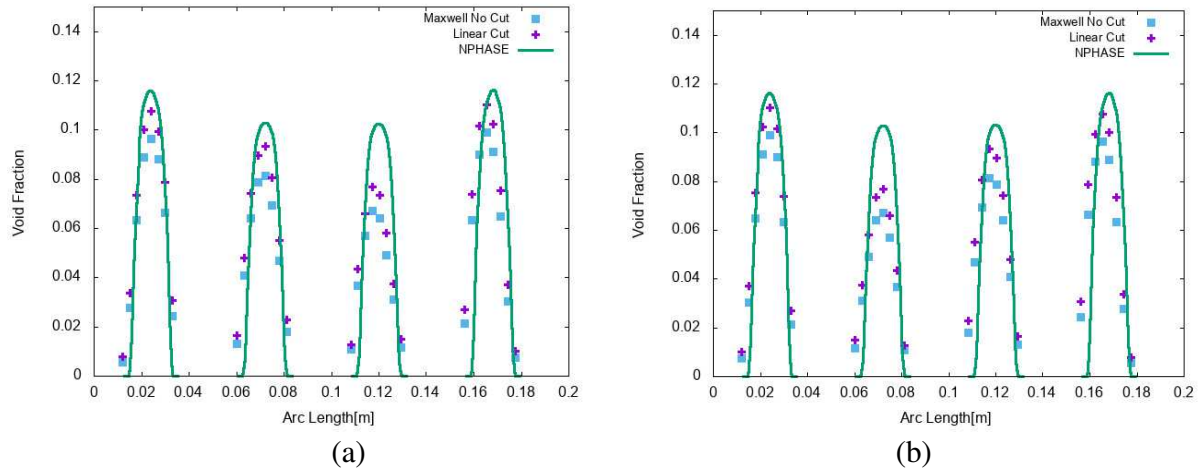


Figure 21. Case 1-3: Void fraction distribution along diagonals with no spacer: (a) diagonal D1, (b) diagonal D2 (see Figure 20 for a location reference).

As can be seen in Figure 16, the relative concentration of large (> 4.9 mm) bubbles upstream from the spacer is about 90% of the total void fraction. Interestingly, the contribution by small bubbles which tend to collect near the rod surfaces is so small that their effect is barely visible in the color contours for all bubbles in Figures 20-23. Thus, given all the combined uncertainties inherently associated with model formulation, using a two-fluid model of deformed-bubbles flow (discussed in Section 3.6) has deemed quite appropriate in the present case.

A thorough examination of the experimental results in Figure 21 indicates that the diagonal distance occupied by the bubbles was about 0.02 m, whereas the corresponding distance between the neighboring rods was slightly over 0.023 m (see Figure 2). The same effect across the entire flow can be seen in Figure 21. Thus the effective area ratio occupied by the bubbles can be estimated at between 0.75 and 0.8 or even lower. On the other hand, for flows in pipes (used in standard two-phase flow experiments), such an area ratio for deformed-bubble flows may be higher than 0.9 (Lucas and Tomiyama, 2011). This in turn, and the fact that the bubbles farther away from the wall flow faster than those near the wall (for the same relative velocity) indicates that relatively narrow gas concentration in the current case will result in the average void fraction lower by 15% to 25% than that predicted when using the drag model in Eq.(18). To account for this effect, the ‘drag-coefficient’-to-‘bubble diameter’ ratio used in the model was reduced from 195 to 160 (about 18%, $C_D=0.8$). Whereas the selected value was only an estimate, its correctness has been confirmed by comparing the calculated assembly-averaged void fraction for Case 1-3 (about 3.6%) against the experimental values. This is shown in Figure 6.

The results of calculations using the present model are also shown in Figure 20 and 21. As can be seen in Figure 20, the model correctly picks up the center-peaked void distributions in all subchannels, although the peaks are slightly over-estimated. The line plots in Figure 21 show nearly-symmetric void distributions across the individual sub-channels, very similar to the experimental data. Interestingly, both results indicate that higher void peaks occur in the peripheral subchannels along both diagonals. This trend reflects the impact of the wall boundary conditions in the rod gaps of the outer channels of the assembly, both physical and computational. Overall, the agreement between experiments and simulations is quite good.

The results from the simulation without spacers have again been set as the inlet for the cases with spacer grids. As shown in Figure 18 and 19, while the contribution by smaller bubbles has

increased after the spacer grids due to the effect of breakup, the bubbles greater than the estimated threshold (>4.9 mm) still make up 80 to 90 percent of the total void fraction. Thus, the assumptions discussed in Section 3.6 are still applicable, although the results of calculations are going to be less accurate. Both the experimental and modeling results are shown in Figures 22 through 23.

As in Case 1-1, the experimental and calculated color contours of void fraction at two locations, 50 mm and 250 mm downstream from the spacer, are given in Figure 22. As can be seen, the effect of mixing vanes, spreading the originally center-peaked void fraction, is captured well in the regions close to the spacer (50 mm downstream). The return to the center-peaked-configuration trend is also predicted at the 250 mm location, although it is apparently slower in the calculation than in the experiment, especially in the inner subchannels.

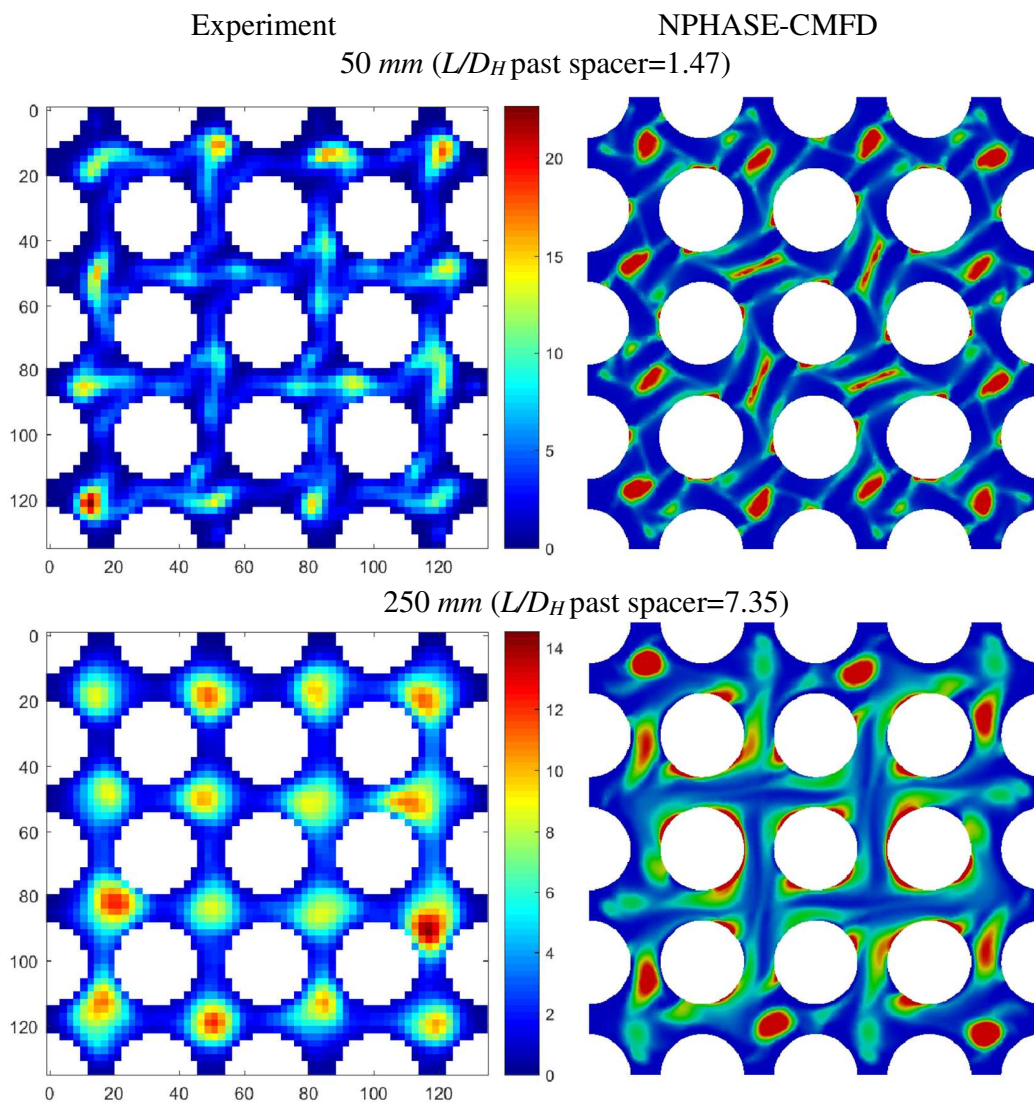


Figure 22. Case 1-3: Void fraction distribution comparison between simulation and experiments with spacer at 50 mm and 250 mm locations downstream from the spacer (scale in percent void). The experimental color contours have been generated using the “Maxwell No Cut” method of data processing.(length units are mm)

Figure 23 shows that a similar trend continues at 450 mm and 650 mm downstream, although the void in the central subchannels returns close to the center-peaked pattern faster in the experiment than in the simulation. This again points to some of the still-open issues concerning how the currently selected modeling parameters affect the distance along the flow required to return to fully-developed conditions. Such issues include the impact of the spacer on the shape of larger bubbles and the model's ability to bring fast enough the gradually distributed void fraction at the exit of the spacer back to the center-peaked shape. Another factor affecting the accuracy of simulations, which is not accounted for in the model, is the increasing contribution by small nearly-spherical bubbles when moving further downstream from the spacer (see Figure 17).

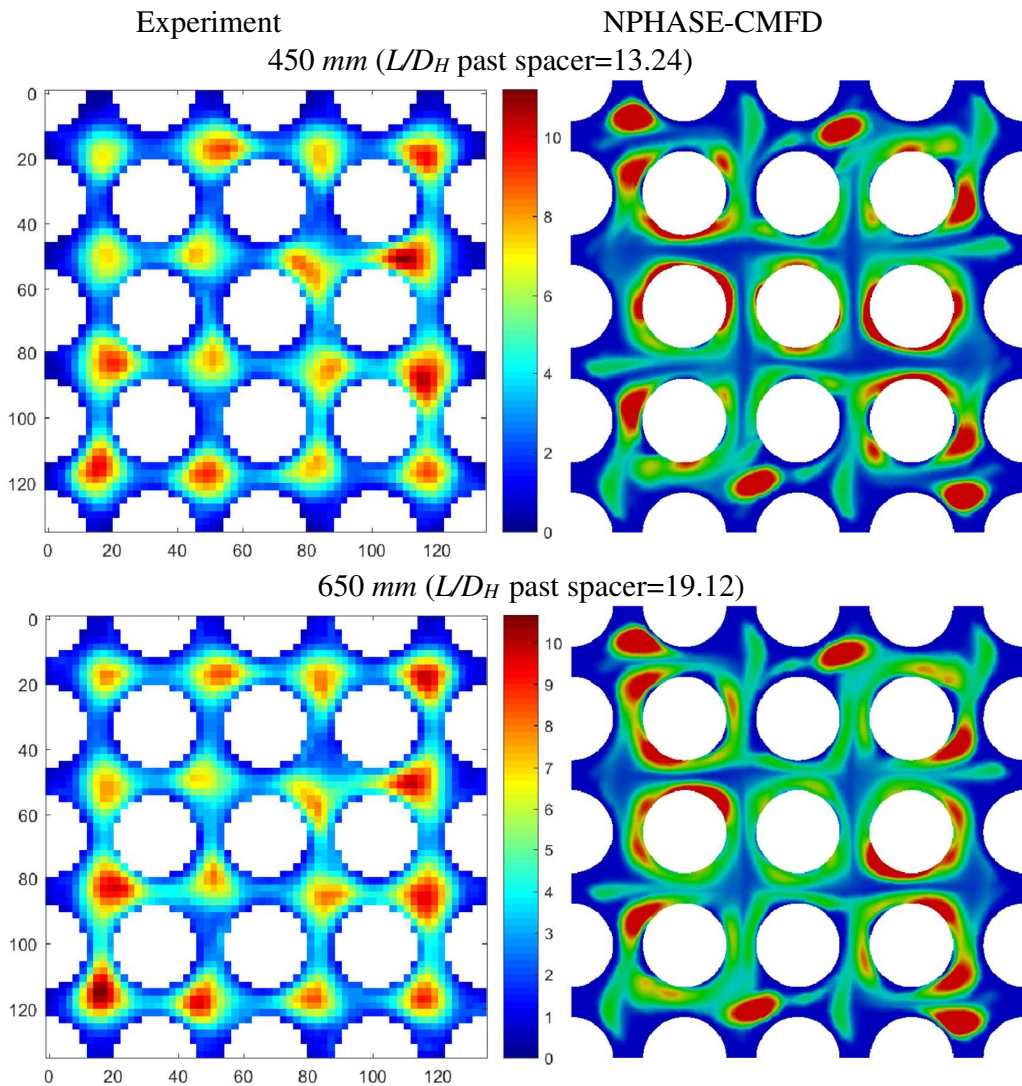


Figure 23. Case 1-3: Void fraction distribution comparison between simulation and experiments with spacer at 450 mm and 650 mm locations downstream from the spacer (scale in percent void). The experimental color contours have been generated using the “Maxwell No Cut” method of data processing. (length units are mm)

An unexpected experimental flow pattern can be observed by examining the transition in the lateral void distribution between 250 mm (Figure 22) and 650 mm (Figure 23). Specifically, whereas a center-peaked distribution similar to the conditions in Figure 19 can be seen at 250 mm, the effect of gradual void spreading between the subchannels can be clearly seen at 450 mm and 650 mm. One possible explanation is due to a weak but persistent effect of the spacer-induced secondary flows around the rods. Interestingly, a trace of similar trend can be seen in the results of calculations, which again confirms the overall physical consistency of the model.

It is interesting to notice that whereas the spacer causes breakup of large bubbles, immediately downstream from the spacer nearly all bubbles still concentrate near the centers of the subchannels. This is mainly due to the effect of turning blades on pushing the liquid phase toward the rods. However, as the distance from the spacer increases, the center peaks become less pronounced and the void gradually spreads over most of the flow area.

The void plots and data points across the diagonals of the rod bundle at a distance of 50 mm downstream from the spacer are presented in Figure 24. As can be seen, the calculated and measured void distributions in the four outer-most sub-channels are in a good agreement. As for Case 1-1, both the calculation and experiment show again local near-wall increases along diagonal D1, which can also be seen in the color images in Figure 22.

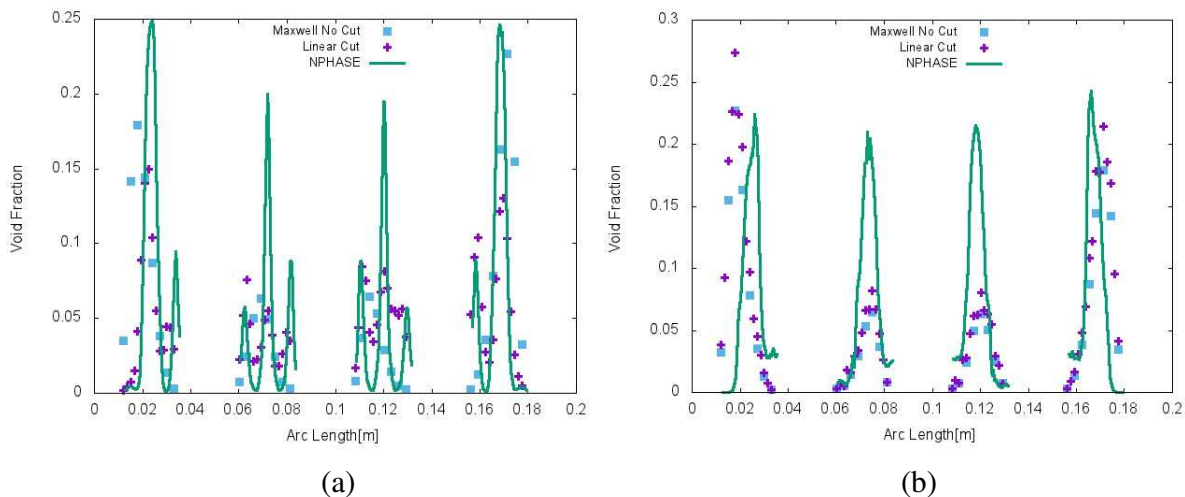


Figure 24. Case 1-3: Void fraction distribution 50 mm downstream from the spacer: (a) diagonal D1, (b) diagonal D2 (see Figure 19 for a location reference).

Both the experiment and the calculation indicate higher void fraction peaks in the peripheral sub-channels as compared to the internal channels. However, in the internal channels the calculation shows higher void peaks than those in the experiment. Those peaks are consistent with the narrow strips of higher void predicted by NPHASE-CMFD at the same axial location, as seen in Figure 22. They are the leftovers of the center-peaked distribution at the inlet to the spacer. The observed differences also reflect the effect of complex spacer geometry on bubble shape, which contributes to the uncertainties of model's predictions.

At the same time, the orientation and shape of the mixing vanes explain the reason why the local peaks in the internal channels along the D1 diagonal are very narrow and those along the other diagonal are relatively wide. An examination of the color contours at 50 mm shows that the subchannel area-averaged void fractions in the internal subchannels from the calculation agree reasonably well with the data. Overall, the same model has been applied to two different cases

and produced consistent results. The results of simulations confirm physical consistency of the overall model and show varying degrees of agreement, from quite good to only reasonable, against the experimental data. The observed differences are due to the combined effects of modeling assumptions and experimental uncertainties. Details of such uncertainties and their quantification are discussed in Section 2 and in Section 3. Specifically, it can be seen that the order of magnitude of most differences, and thus the accuracy of predictions, is compatible with the discrepancies in the experimental results caused by the different data processing methods, and the limitations of selected modeling assumptions. The modeling decisions can only be influenced by what is known in the experiment, and the current results demonstrate that the present modeling assumptions properly capture major trends governing the complex flow and gas concentration patterns in multiple-rod assemblies with turning-vane spacer grids.

6. Conclusions

Local patterns of two-phase flow in the complex geometry of a square rod bundle with spacer grid have been analyzed both experimentally and using a computational model. Two methods of processing the raw experimental data from a wire-mesh sensor have been discussed: the “Linear Cut” method which has been used before, and a newly introduced “Maxwell No Cut” method. It has been shown that the new method is more consistent and its overall accuracy has been confirmed by comparing the average measured void fraction with a drift flux model that was validated against the existing database for flow along smooth rod bundles w/o spacers.

The model has been based on the ensemble-averaged RANS-level two-phase flow multi-field conservation equations, and has been encoded in the NPHASE-CMFD computer solver. The objective of the study was to analyze two specific SUBFLOW experiments, each pertaining to different flow conditions and thus requiring a different modeling approach. Specifically, Case 1-1 represents a low volumetric gas flow fraction of small dispersed bubbles, whereas Case 1-3 deals with a higher gas flow and large predominantly deformed bubble.

It is well known that gas/liquid flows cover a broad spectrum of patterns (or regimes). Even at low relative gas superficial velocities, bubbles of different sizes can frequently be observed. Whereas the multi-field modeling concept is applicable to poly-dispersed bubbly flows, the formulation of a complete model for such situations requires that several closure laws be used which normally involve a large number of adjustable parameters. Consequently, model validation involves a lot of tuning. This, in turn, normally leads to increasing uncertainties of the predictions with the increasing level of model complexity. Consequently, it is important that model formulation be based on a thorough analysis of dominant phenomena, limiting the number of adjustable constants and secondary-level closure laws.

The basic factor behind modeling the differences between Case 1-1 and Case 1-3 was the bubble size relative to the threshold value, which affects the direction of lift force. Based on examining the available evidence, including both physical and virtual experiments, it has been concluded that for the SUBFLOW experimental conditions the critical bubble diameter, beyond which the shape distortion occurs, is less than 5 mm.

The analysis of the measured bubble size distribution for Case 1-1 revealed that the majority of bubbles were of 3 mm to 4 mm diameter range, with an average value of 3.73 mm and a standard deviation of 0.62 mm. For such a magnitude and narrow range of bubble sizes, it has been concluded that the most appropriate and consistent approach is to use a two-fluid model of monodispersed bubbles. A comparative analysis between the computer simulations and the measured values has provided results that reflect the effect of the complex flow pattern induced

by the presence of the spacer grid. Phenomena such as the accumulation of small bubbles close to the surface of solid rods, their transport to the center of the subchannels due to the swirl induced by the spacer vanes, and their return to the walls accompanying the decay of the swirl with a growing downstream distance have been predicted qualitatively quite well, whereas the quantitative discrepancies in most calculations have been maintained within reasonable practical limits. Some of the experimental findings, such as the azimuthal non-uniformity of the void fraction distribution around the rods at low gas concentrations could not be reproduced by the model since they are very likely due to manufacturing tolerances of the gas-injection device, geometry interactions, and accuracy limits imposed by the wire mesh dimensions on small bubble detection.

In Case 1-3, carrying out a consistent comparison between the calculation and the experiment has been a more complicated task, mainly due to the uncertainties associated with the modeling of drag and lift forces. The fact that the drag force for deformed bubble flows is primarily a function of the ratio of drag coefficient to bubble diameters allowed the rationalization of the use of a two-fluid model in this case as well. However, several other factors affected the accuracy of predictions, the most important of which include: the fact that the existing expressions for the drag coefficient are based on area-averaged parameters, the range of experimentally-observed bubble deformation criteria, and the range of proposed values for the lift coefficient after the transition. In comparison to the above, ignoring the presence of a low fraction of small bubbles had a negligible effect on the results. Nonetheless, the structures directly induced by the complex geometrical boundary conditions imposed by the spacer grid and its vanes have been predicted quite well in the region at a short distance downstream of the spacer grid. Further downstream, the deviations become larger, since here the swirl gradually decays off and the interfacial force balance takes over as the main structure-governing effect.

Among the quantitative findings, it is remarkable that the model can reproduce the slightly higher void peaks in the corner subchannels of the experimental bundle. On the other hand, a certain overestimation of the void fraction peaks by the calculations is notable, since it cannot be attributed to the measuring uncertainty of the wire-mesh sensor. Nevertheless, the calculated average void fraction has agreed well with the measurements.

The major findings of the current study include the following:

- Experimental confirmation that the proposed models of interfacial forces, which are normally used for gas/liquid flow in circular pipes, are still applicable in the modeling of lateral void distribution in multiple rod assemblies.
- Confirmation of the effect of dominant bubble size on void distribution.
- Confirmation that the wire mesh sensor is capable of capturing the effect of spacer on bubble size distribution.
- Theoretical explanations of the impact of complex-geometry spacer grids on local flow field and phase distribution.

Discussion of the importance of assessing the modeling uncertainties (or imperfection) on proper interpretation of the combined results of measurements and simulations.

As mentioned above, the main theoretical and computational goals of this work have been to demonstrate that the current model is capable of reproducing the major experimental trends associated with the impact of the spacer with mixing vanes on the flow field and phase distribution in a multiple-rod assembly for two cases, one of which pertains to small spherical bubbles (Case 1-1), the other to predominantly large deformed bubbles of different sizes (Case 1-3). The common feature of both cases is the applicability of a two-field model. Needless to

say, the current model can be extended in the future to a multi-field multiple bubble-group format, and be used to analyze two-phase flows which involve a broad spectrum of bubble sizes, such as those observed in some of the other SUBFLOW experimental cases listed in Table 1. However, future studies should also address the following issues:

- Enhanced model's ability to account for the effect of swirling liquid flows on transition to fully-developed conditions downstream from the spacer.
- The effect of possible bubble-bubble interactions (coalescence and/or breakup) on local void fraction downstream from the spacer.
- The effect of spacers of various geometries on bubble shape.

Whereas the advantages of the multi-field concept of modeling two-phase flows are commonly recognized, including its computational efficiency and applicability to a wide range of complex system geometries and operating conditions, the predictive capabilities of such a class of models can, and should, be still improved. It is anticipated that a meaningful progress can be made in both our understanding of the underlying two-phase flow physics in general, and in enhancing the accuracy of predictions for complex two-phase systems in particular, by using novel experimental techniques combined with virtual experiments based on DNS/Interface-Tracking simulations to develop new and improved mechanistic ensemble-averaged closure laws compatible with the multi-field conservation equations.

Acknowledgments

This research was performed under the appointment of the first author as a recipient of the Rickover Fellowship Program in Nuclear Engineering sponsored by Naval Reactors Division of the U.S. Department of Energy. The authors would also like to thank the CASL program of the U.S. Department of Energy for their support.

Nomenclature

| | |
|------|-------------------------------------|
| d | diameter |
| g | Gravity |
| I | Conductivity |
| j | Superficial Velocity |
| k | Turbulent Kinetic Energy |
| M | Interfacial Momentum Transfer Terms |
| P | Pressure |
| Re | Reynolds Number |
| u | Velocity |
| v' | Fluctuating velocity |

Greek Symbols

| | |
|---------------|------------------------------|
| α | Void Fraction |
| β | Kinematic void concentration |
| ε | Turbulence Dissipation Rate |
| ρ | Density |
| τ | Shear |
| σ | Surface Tension |
| ν | Kinematic Viscosity |

Superscripts and Subscripts

| | |
|-----------|----------------------|
| <i>b</i> | bubble |
| <i>D</i> | Drag |
| <i>k</i> | Phase indicator |
| <i>l</i> | Liquid |
| <i>L</i> | Lift |
| <i>v</i> | vapor |
| <i>r</i> | relative |
| <i>TD</i> | Turbulent Dispersion |
| <i>VM</i> | Virtual Mass |

References

- Alajbegovic, A., Kurul, N., Podowski, M.Z., Drew, D.A., Lahey, Jr., R.T., 1996. A CFD analysis of multidimensional phenomena in two-phase flow using a two-fluid model, In: Proc. ANS. 1996 National Heat Transfer Conference, HTC-Vol. 9, 387-396.
- Anglart, H., Nylund, O., Kurul, N., Podowski, M.Z., 1997. CFD Simulation of Flow and Phase Distribution in Fuel Assemblies with Spacers, Nuclear Engineering and Design, 177, 215-228.
- Antal, S.P., Ettorre, S.M., Kunz, R.F., Podowski, M.Z., 2000. Development of a next generation computer code for the prediction of multicomponent multiphase flows, in: Proc. Int. Meet. Trends Num. Phys. Model. Ind. Multiph. Flow, Cargese, France, 1-10,
- Antal, S.P., Podowski, M.Z., Lahey, R.T., Jr., 2001. On the Multidimensional Modeling of Annular Two-Phase Flows around Spacers", Proc. of the 4th Int. Conference on Multiphase Flow, ICMF'2001, New Orleans, LA.
- Antal, S.P., Hu, M.H., Podowski, M.Z., 1998. CFD Analysis of Two-Phase Flow Around Tube Support Plates in U-Tube Steam Generators. Proc. 6th International Conference on Multiphase Flow in Industrial Plants, Milan, Italy.
- Antal, S.P., Hu, M.H., Podowski, M.Z., 2003. Multidimensional Modeling of Annular Flows in Complex Geometries and BWR Fuel Assemblies. Proc. Tenth International Topical Meeting on Nuclear Reactor Thermal Hydraulics (NURETH-10), Seoul, Korea.
- Behafarid, F., Jansen, K.E., Podowski, M.Z., 2015. Theoretical and Computational Study on Large Bubble Motion and Liquid Film in Inclined and Vertical Narrow Conduits, Int. J. Multiphase Flow 75, 288-299.
- Behafarid, F., Shaver, D., Bolotnov, I.A., Antal, S.P., Jansen, K.E., Podowski, M.Z., 2013. Coupled DNS/RANS Simulation of Fission Gas Discharge during Loss-of-Flow Accident in Gen-IV Sodium Fast Reactor, Nuclear Technology 181, 44-55.
- Bolotnov, I. A., Antal, S.P., Jansen, K.E., Podowski, M.Z. 2012. Multidimensional Analysis of Fission Gas Discharge following Fuel Element Failure in Sodium Fast Reactor, Nuclear Engineering and Design, 247, 136-146
- Bolotnov, I. A., Podowski, M.Z., 2012. Investigation of Turbulence in Bubbly Gas/Liquid Flows using Interface Tracking Simulations, In: Proc. Embedded Topical Meeting: Advances in Thermal-Hydraulics, 2012 ANS Winter Meeting, San Diego, CA 29-37.
- Bolotnov, I.A., Jansen, K.E., Drew, D.A., Oberai, A.A., Lahey, Jr., R.T., Podowski, M.Z., 2010. Detached Direct Numerical Simulations of Turbulent Two-Phase Bubble Channel Flow, International Journal of Multiphase Flow 37, 647-659.
- Busco, G., Hassan, Y. A., 2018. Space and energy-based turbulent scale-resolving simulations of flow in a5x5 nuclear reactor core fuel assembly with a spacer grid, International Journal of Heat and Fluid flow 71, 420-441.

- Busco, G., Merzari, E., Hassan, Y. A., 2019. Invariant analysis of the Reynolds stress tensor for a nuclear fuel assembly with spacer grid and split type vanes. *International Journal of Heat and Fluid flow* 77, 144-156.
- Chun, T. H., Oh, D., 1998. A pressure drop model for spacer grids with and without flow mixing vanes, *J. Nucl. Sci. Technol.* 35, 508–510.
- Coddington, P., Macian, R., 2012. A study of the performance of void fraction correlations used in the context of drift-flux two-phase flow models, *Nucl. Eng. Des.* 215, 199–216.
- Conner, M.E., Perez, C.E., Dominguez-Ontiveros, E., Hassan, Y.A., 2016. Demonstration of Advanced Hydraulic Benchmark Data for PWR Mixing Vane Grid, in: *CFD4NRS-6 Workshop*, Cambridge, Ma.
- N. Cinosi, S. Walker, M. Bluck, and R. Issa, 2014, “CFD simulation of turbulent flow in a rod bundle with spacer grids (MATIS-H) using STAR-CCM+,” *Nucl. Eng. Des.*, 279, 37–49
- Chang, S. K., Moon, S. K., Baek, W. P and Choi, Y. D. 2008, “Phenomenological investigations on the turbulent flow structures in a rod bundle array with mixing devices,” *Nucl. Eng. Des.*, 238, 3, 600–609,
- Chen, X., Du, S., Zhan, Y., Hongxing, Y., Li, S., Peng, H., Wang, W., Zeng, W. 2017, “Validation of CFD analysis for rod bundle flow test with vaned spacer grids,” *Ann. Nucl. Energy*, 109, 370–379
- Delhaye, J.M., 1981. *Basic Equations for Two-Phase Flow Modeling*, Two-Phase Flow and heat transfer in the Power and Process Industries, A.E. Bergles et al., Eds., Hemisphere Publishing, Washington
- Dominguez Ontiveros, E., Hassan, Y. A., Conner, M. E., Karoutas, Z. E., 2012. Experimental benchmark data for PWR rod bundle with spacer-grids, *Nucl. Eng. Des.* 253, 396–405,
- Drew, D., Cheng, L., Lahey Jr., R. T., 1979. The analysis of virtual mass effects in two-phase flow, *Int. J. Multiph. Flow* 5, 233–242.
- Eichhorn, R., Small, C. S., 1964. Experiments on the lift and drag of spheres suspended in a Poiseuille flow, *J. Fluid Mech.* 20, 513-527.
- Ervin, E. A., Tryggvason, G., 1997. The rise of bubbles in a vertical shear flow, *J. Fluids Eng.* 119, 443–449.
- Feng, J., Bolotnov, I. A., 2017. Interfacial force study on a single bubble in laminar and turbulent flows, , *Nucl. Eng. Des.* 313, 345–360.
- Galloway, T., Antal, S.P., Podowski, M.Z., Guillen, D., 2007. NPHASE Predictions of Turbulent Flow in the Lower Plenum of a Prismatic Gas-Cooled Reactor, *Proc. 12th International Topical Meeting on Nuclear Reactor Thermal-Hydraulics (NURETH-12)*, Pittsburgh, PA.
- Goodheart, K., Ylönen, A., De Cacqueray, V.D., Prasser, H-M. 2014. CFD Validation of Void Distribution in a Rod Bundle with Spacer, In: *Proc. 2014 22nd International Conference on Nuclear Engineering*.
- Holloway, M. V., Conover, T. A., McClusky, H. L., Beasley, D. E., Conner, M. E., 2005. The effect of support grid design on azimuthal variation in heat transfer coefficient for rod bundles, *J. Heat Transfer* 127, 598–605.
- Ishii, M., Mishima, K., 1984. Two-fluid model and hydrodynamic constitutive relations, *Nucl. Eng. Des.* 82, 107–126.
- Jiao, H., Podowski, M. Z., 2012. An analysis of multidimensional models of gas/liquid flows, In: *Trans. Am. Nucl. Soc.*, 103, San Diego, CA, 1393–1394,
- Karoutas, Z. E., Gu, C., Sholin, B., 1995. 3-D flow analyses for design of nuclear fuel spacer, in: *Proc. 7th Int. Topical Meeting on Nucl. Reactor Thermal-Hydraulics (NURETH-7)*, Saratoga, NY, 3153–3174.
- Kurul, N., Alajbegovic, A., Podowski, M.Z., 1996. Multiphase modeling in CFX 4, In: *Proc. Int. CFX Users Conference*, London, England

- Kurul, N., Podowski, M.Z., 1988. Grid generation for the analysis of dispersed-phase motion in two-phase flows, in *Numerical Grid Generation in Computational Fluid Mechanics*, Pineridge Press, 1988.
- Kurul, N., Podowski, M.Z., 1996. Predictions of Fuel Overheating in Partially Blocked Narrow reactor Channels Using Multidimensional Models, *ANS Proc. 31 National Heat Transfer Conference, HTC-Vol. 9*, 405-416
- Lahey, Jr., R.T., Drew, D.A., 1988. The three dimensional time- and volume averaged conservation equations of two-phase flow, *Advances in Nuclear Science and Technology*, 20, 1-69.
- Liao, L.H., Parlos, A., Griffith, P., 1985. Heat transfer, carry-over and fall back in PWR steam generators during transients, *NUREG/CR-4376,EPRINP-4298*
- Liu, C. C., Ferng, Y. M. and Shih, C. K., 2012, "CFD evaluation of turbulence models for flow simulation of the fuel rod bundle with a spacer assembly," *Appl. Therm. Eng.*, 40, 389–396
- Lucas, D., Tomiyama, A., 2011. On the role of the lateral lift force in poly-dispersed bubbly flows. *Int. J. Multiphase Flow* 37, 1178-1190.
- McClusky, H. L., Holloway, M. V., Conover, T. A., Beasley, D. E., Conner, M. E., Smith, L. D., 2003. Mapping of the lateral flow field in typical subchannels of a support grid with vanes, *J. Fluids Eng.* 125, 987–996.
- Milenković, R., 2005. Experimental investigation of bubbly jets, Ph.D. dissertation, Lab. of Nucl. Eng., ETH-Zurich, Zurich, Switzerland.
- Navarro, M. A. and Santos, A., 2009. Numerical evaluation of flow through a 5x5 PWR rod bundle: Effect of the vane arrangement in a spacer grid, Presented at the 2009 Int. Nucl. Atl. Conf., Rio de Janeiro, Brazil.
- Nguyen, T., Hassan, Y. , 2017. Stereoscopic particle image velocimetry measurements of flow in a rod bundle with a spacer grid and mixing vanes at a low Reynolds number, *International Journal of Heat and Fluid Flow*, 67, 202-219
- Podowski, M. Z., 2009. On the consistency of mechanistic multidimensional modeling of gas/liquid two-phase flows, *Nucl. Eng. Des.* 239, 933–940.
- Podowski, M.Z., 2019a, Is Reactor Multiphase Thermal-Hydraulics a Mature Field of Engineering Science? *Nucl. Eng. Des.* 345, 196-208.
- Podowski, M.Z., 2019b, Understanding Two-Phase Flow and Boiling Heat Transfer: Challenges and Paradoxes, *Nucl. Eng. Des.*, doi 110185, 1-10.
- Podowski, M.Z., Shaver, D.R., 2013. Recent advancements in multidimensional modeling of two-phase flow and heat transfer in reactor fuel assemblies, *Proc. International Seminar on Subchannel Analysis, CFD Modeling and Verification, CHF Experiments and Benchmarking*, Xi'an, China.
- Pointwise User Manual, Pointwise Inc., 2011. Fort Worth, TX,
- Prasser, H.M., Häfeli, R., 2018. Signal response of wire-mesh sensors to an idealized bubbly flow. , *Nucl. Eng. Des.* 336, 3–14.
- Prasser, H.M., Misawa, M., Tiseanu, I., 2005. Comparison between wire-mesh sensor and ultra-fast X-ray tomography for an air water flow in a vertical pipe, *Flow Meas. Instrum.* 16, 73–83.
- Prasser, H.M., Scholz, D., Zippe, C., 2001. Bubble size measurement using wire-mesh sensors, *Flow Meas. Instrum.* 12, 299–312.
- Sato, Y., Sadatomi, M., Sekoguchi, K., 1981. Momentum and heat transfer in two-phase bubble flow-I, *Int. J. Multiph. Flow* 7, 167–177.
- Shaver, D.R., Antal, S.P., Podowski, M.Z., 2013. Modeling and Analysis of Interfacial Heat Transfer Phenomena in Subcooled Boiling along PWR Coolant Channels, *Proc. 15th Int. Topical Meeting on Nuclear Reactor Thermal-hydraulics (NURETH-15)*, Pisa, Italy.
- Shaver, D.R., Podowski, M.Z. 2015. "Modeling and Validation of Forced Convection Subcooled Boiling", In: *Proc. 16th Int. Topical Meeting on Nuclear Reactor Thermal-hydraulics (NURETH-16)*, Chicago, Il., Aug. 30-Sep. 4,

- Tiwari, P., Antal, S. P., Podowski, M. Z., 2006. Three-dimensional fluid mechanics of particulate two-phase flows in U-bend and helical conduits, *Phys. Fluids* 18, 1–18.
- Tomiyama, A., Tamai, H., Zun, I., Hosokawa, S., 2002. Transverse migration of single bubble in simple shear flows, *Chem. Eng. Sci.* 57, 1849–1858.
- Tompkins, C., Prasser, H.M., Corradini, M., 2018. Wire-mesh sensors: A review of methods and uncertainty in multiphase flows relative to other measurement techniques, *Nuclear Engineering and Design* 337, 205-220
- Tselishcheva, E.A., Antal S.P., Podowski, M.Z., 2010. Mechanistic Multidimensional Analysis of Horizontal Two-phase Flows, *Nuclear Engineering and Design*, 240, 405-415.
- Waite, B. M., Shaver, D. R., Podowski, M. Z., 2012. Multidimensional Analysis of Flow through Sudden Expansions and Contractions in Pipes, *ANS Transactions*, 2012 Winter Meeting, San Diego, CA, November, 1336-1368.
- Waite, B. M., Shaver, D. R., Podowski, M. Z., 2014. Multidimensional mechanistic modeling of fluid flow and heat around spacer grids, in: *Proc. Int. Cong. Adv. in Nucl. Power Plants (ICAPP)*, Charlotte, NC, 124–133
- Waite, B. M., 2018. *Mechanistic Modeling of Two-Phase Flow and Heat Transfer Around Light Water Reactor Spacer Grids*, Ph.D. dissertation, Mechanical, Aerospace and Nuclear Engineering, Rensselaer Polytechnic Institute, Troy, NY
- Wang, S.K., Lee, S.J., Jones, O.C., Lahey, Jr., R.T., 1987. 3-D turbulence structure and phase distribution measurements in bubbly two-phase flows, *Int. J. Multiphase Flow* 13, 327-343.
- Ylönen, A., 2013. *High-resolution flow structure measurements in a rod bundle*, Ph.D. dissertation, Lab. of Nucl. Eng., ETH-Zurich, Zurich, Switzerland,
- Ylönen, A., Bissels, W.M., Prasser, H.M., 2011, Single-phase cross-mixing measurements in a 4x4 rod bundle, *Nucl. Eng. Des.* 241, 2484–2493.
- Yuan, P, Yan, J., Xu, Y. and Karoutas, Z. E, 2013“Comparison between CFD analysis and experimental data for flow in a 5x5 rod bundle with spacer-grids,” in *Trans. Am. Nucl. Soc.*, vol. 109, Washington, DC, 2013, 1605–1608.
- Zuber, N., Findley, J.A., 1965. Average Volumetric Concentration Two-Phase Flow Systems. *J. Heat Transfer* 87, 453